Bioactive Materials 54 (2025) 329–351

Contents lists available at ScienceDirect

Bioactive Materials

journal homepage: www.keaipublishing.com/en/journals/bioactive-materials

Hydrogel scaffold encapsulating MSC-Exos and ZIF-8 promotes bone regeneration via coordinating osteogenesis and immunomodulation

Yunhui Si [a], Xiaorong Li [b], Shuao Dong [a], Xueqin Gao [a], Yuetong Zhu [b], Linzhen Mo [b], Zhiwei Wang [c], Shuhan Wang [d,*], Chao Zhang [a,**]

[a] School of Biomedical Engineering, Shenzhen Campus of Sun Yat-sen University, Shenzhen, Guangdong, 518107, PR China
[b] The Seventh Affiliated Hospital of Sun Yat-sen University, Shenzhen, Guangdong, 518107, PR China
[c] Southern Marine Science and Engineering Guangdong Laboratory (Zhuhai), Zhuhai, Guangdong, 519000, PR China
[d] Shenzhen Institute for Drug Control, Shenzhen Testing Center of Medical Devices, Shenzhen, Guangdong, 518057, PR China

ARTICLE INFO

Keywords:
MSC-Exos
ZIF-8
Hydrogel
Osteogenesis
Immunomodulation

ABSTRACT

The limited bone regeneration and suboptimal immune responses constitute the major challenges in repairing critical-sized bone defects. As an emerging therapeutic modality, mesenchymal stem cell-derived exosomes (MSC-Exos) exhibit promising application prospects in bone regeneration. In this study, the bone-functionalized MSC-Exos are loaded into GelMA hydrogel scaffolds modified with the bone immunomodulator Zeolitic Imidazolate Framework-8 (ZIF-8) for the repair of critical-sized bone defects. The prepared MSC-Exos/ZIF-8@GelMA composite hydrogel demonstrates excellent biocompatibility and favors the adhesion and proliferation of bone marrow mesenchymal stem cells (BMSCs). The sustained release of exosomes and zinc ions endows the composite hydrogel with synergistically enhanced bone regeneration, angiogenesis, and immunomodulation. Specifically, the microRNA-23a-3p within internalized MSC-Exos activates the AKT signaling pathway in BMSCs by targeting the PTEN node and up-regulates the expression of osteogenesis-related markers. Meanwhile, it is demonstrated for the first time that ZIF-8 inhibits the activation of the non-classical NF-κB pathway in RAW264.7 cells under simulated inflammatory conditions, thereby downregulating pro-inflammatory cytokine expression and inducing M2-type polarization. The rat cranial bone defect model demonstrates that the composite hydrogel significantly enhances new bone formation and angiogenesis *in vivo* and maintains a low level of inflammation. The design of a composite hydrogel featuring synergistic enhancement of osteogenesis and immunomodulation represents a novel strategy for developing bone tissue engineering scaffolds.

1. Introduction

Repair of large-sized bone defects resulting from severe injury, open fractures, bacterial infections, tumor resection, or congenital genetic disorders constitutes a global clinical challenge [1–3]. Artificial bone offers new possibilities for bone regeneration by mimicking the structure and function of autologous bone [4,5]. In clinical practice, artificial bone graft materials have significant advantages over autogenous or allogeneic bone in terms of avoiding secondary trauma and pain, unlimited supply, reduced surgical complexity and infection risk. The rapid advancement of bone tissue engineering (BTE) has significantly promoted the development of artificial bone grafting materials [6,7]. BTE scaffolds consisting of matrix, seed cells, and bioactive factors can replicate the intricate structure and biological roles of natural bones while adjusting the physical and chemical characteristics in response to the evolution of the *in vivo* microenvironment [8].

In recent times, stem cell-derived exosome-based therapeutic strategies have garnered substantial attention in the field of regenerative medicine [9–11]. Exosomes are naturally occurring nanovesicles that facilitate intercellular communication via paracrine or other signaling pathways [12]. The phospholipid bilayer of exosomes encapsulates a multitude of bioactive substances, including proteins, lipids, and nucleic acids (such as miRNA, lncRNA, circRNA, tsRNA, and mRNA), which serve essential functions in intercellular communication [13]. In

Peer review under the responsibility of editorial board of Bioactive Materials.
* Corresponding author.
** Corresponding author.
E-mail addresses: wangshuhan@szidc.org.cn (S. Wang), zhchao9@mail.sysu.edu.cn (C. Zhang).

https://doi.org/10.1016/j.bioactmat.2025.08.026
Received 20 April 2025; Received in revised form 10 July 2025; Accepted 18 August 2025
Available online 25 August 2025

contrast to implanted cells, exosomes are inherently non-immunogenic, signifying that they do not trigger an immune rejection response following implantation, thereby significantly enhancing the safety of the treatment [14]. Additionally, research has shown that exosomes do not express MHC class I or II antigens and are non-self-replicating [15]. This, in turn, serves to lower the risk of iatrogenic tumor formation. A growing body of evidence indicates that the secreted exosomes dominate the beneficial effects of implanted MSCs on bone reconstruction [16,17]. These MSC-Exos motivate the inherent receptor cells rather than directly differentiating into parenchymal cells for tissue repair [18,19]. The miRNAs carried by MSC-Exos specifically bind to mRNA in target cells, inhibiting post-transcriptional gene expression and consequently influencing physiological functions, including osteoblast proliferation, differentiation, and apoptosis [20–24]. Furthermore, MSC-Exos reduces the expression of proinflammatory cytokines in immune cells, thereby diminishing inflammation-induced delays in bone healing and promoting bone tissue regeneration [25,26]. Consequently, integrating MSC-Exos into biological scaffolds represents an ideal option for achieving effective bone tissue repair.

Tissue injury, healing, and regeneration within the musculoskeletal system involve intricate inflammatory processes, and MSCs and their exosomes are able to exert anti-inflammatory effects by modulating the inflammatory microenvironment [27]. Nevertheless, the miRNA profile of MSC-Exos undergoes changes during the osteogenic differentiation of MSCs as a result of gene expression reprogramming and organelle redistribution [28,29]. The alterations in miRNA profiles in MSC-Exos may produce novel or unanticipated immunomodulatory effects. Previous investigations have demonstrated that miR-18a-5p within MSC-Exos targets ATM to activate the p53 pathway and induce a high level of M2 macrophage polarization [30]. However, the immunomodulatory function of MSC-Exos significantly declines when BMSCs undergo differentiation into osteoblasts. The instability of the immunomodulatory capacity of MSC-Exos makes it challenging to fully satisfy the therapeutic requirements of bone repair in clinical settings [31]. Consequently, additional immunomodulators need to be introduced to synergistically modulate the immune microenvironment and enhance osseointegration for the design of MSC-Exos-based BTE scaffolds.

Drawing motivation from the nanostructures of natural extracellular matrix, mimicking cellular physiology, and precisely modulating cellular behavior through synthetic nanostructures has been widely developed in regenerative medicine [32,33]. Among various nanomaterials, MOFs feature porous structures and mechanical properties analogous to those of substitute tissue, which facilitate cell attachment and growth as well as the exchange of nutrients and metabolites [34]. The osteogenic effects of MOFs have been widely reported, and MOFs can be used as osteoinductive materials, delivering growth factors or drugs and constructing bone graft scaffolds [35–37]. In recent years, MOFs have provided an innovative platform for collaborative osteogenesis and immunomodulation, owing to their unique structural designability, high loading capacity, and controllable release properties [38–40]. The metal nodes within MOF frameworks can progressively dissociate and release ions under physiological conditions, with specific metallic ions possessing well-documented immunomodulatory functions. Simultaneously, organic ligands (such as imidazole derivatives and carboxylic acids) generated through MOF degradation may exhibit inherent bioactivity and participate in immune regulation. Furthermore, the exceptionally large surface area and adjustable pore size of MOFs enable efficient loading of osteoimmunomodulatory factors, while structural modifications, surface functionalization, or stimulus-responsive designs facilitate on-demand drug release for sustained regulation of local immune responses [41]. Among various MOFs, ZIF-8 formed through the coordination between Zn^{2+} and 2-methylimidazole demonstrates superior biocompatibility and maintains structural stability in physiological environments [42]. The incorporated Zn^{2+} serves as an essential trace element in human physiology, participating in osteoblast differentiation and bone matrix mineralization [43]. Concurrently, Zn^{2+} promotes macrophage polarization towards the anti-inflammatory M2 phenotype, inhibits pro-inflammatory cytokines such as TNF-α and IL-1β, and upregulates reparative factors including IL-10 and Arg-1 [44]. Consequently, ZIF-8 has garnered increasing attention as a novel osteoimmunomodulatory agent in bone tissue engineering applications.

Integrating MSC-Exos with immunomodulatory MOFs to synergistically enhance osteogenic effects and create a beneficial bone immune microenvironment is an ideal solution for constructing innovative bone tissue engineering scaffolds. To date, no relevant studies have been reported in bone tissue engineering. We hypothesize that ZIF-8 can address the functional limitations of MSC-Exos in immunomodulation and synergistically enhance the osteogenic properties of bone tissue engineering scaffolds, thereby providing an innovative solution for repairing critical-sized bone defects. Simultaneously, elucidating the underlying molecular mechanisms governing osteogenesis and immune regulation will significantly accelerate the clinical translation of this composite system. In this study, we constructed functional bioscaffolds with accelerated bone regeneration by isolating MSC-Exos from osteogenically pre-differentiated BMSCs through ultracentrifugation and encapsulating them in ZIF-8-modified GelMA hydrogels (Scheme 1). The MSC-Exos internalized by BMSCs can effectively promote osteogenesis-related protein expression and accelerate extracellular matrix mineralization. Furthermore, the incorporation of ZIF-8 further enhances the immunomodulatory capacity of the scaffold and positively induced the transition of RAW264.7 cells from pro-inflammatory to anti-inflammatory phenotype. In the rat cranial defect model, the composite scaffold exhibited remarkable osteoinductive properties, accelerated bone healing, and reduced inflammatory responses. More importantly, this study demonstrates the signaling pathway of miRNA-targeted osteogenesis in MSC-Exos and reveals the potential molecular mechanisms of ZIF-8 as a bone immunomodulator. These findings provide a novel design strategy for bone tissue engineering scaffolds by integrating exosomes with immunomodulators to accelerate bone regeneration.

2. Materials and methods

2.1. Identification of BMSCs

Flow cytometry was utilized to evaluate the purity of BMSCs. In brief, BMSCs were harvested using trypsin-EDTA, rinsed with PBS, and subsequently incubated with fluorescence-labeled antibodies specific for positive surface markers (CD44-PE and CD90-FITC) and negative markers (CD34-APC and CD45-PerCP) for 30 min at 4 °C in the dark. Following a washing step, the cells were analyzed using a flow cytometer (Beckman, USA), and the acquired data were processed using FlowJo software (TreeStar, USA). The cell purity was assessed based on the expression levels of CD44 (BioLegend, USA) and CD90 (BioLegend, USA) as positive markers, and CD34 (BioLegend, USA) and CD45 (BioLegend, USA) as negative markers, in accordance with the criteria established by the International Society for Cellular Therapy (ISCT) [45]. To further confirm the identity of BMSCs, their tri-lineage differentiation potential was evaluated under specific induction conditions. Osteogenic differentiation was induced in α-MEM supplemented with 10 % fetal bovine serum (FBS), 0.1 μM dexamethasone, 50 μM L-ascorbic acid, and 10 mM sodium β-glycerophosphate; adipogenic differentiation was induced in DMEM containing 10 % FBS, 0.5 mM isobutylmethylxanthine, 1 μM dexamethasone, 10 μM insulin, and 200 μM indomethacin; chondrogenic differentiation was induced in high-glucose DMEM supplemented with 1 % ITS + premix, 0.1 mM sodium pyruvate, 50 μM ascorbic acid, and 10 ng/mL TGF-β3. After 21 days of induction, osteogenic differentiation was verified by Alkaline Phosphatase (ALP) staining and Alizarin Red S (ARS) staining, adipogenic differentiation was confirmed by Oil Red O staining for lipid

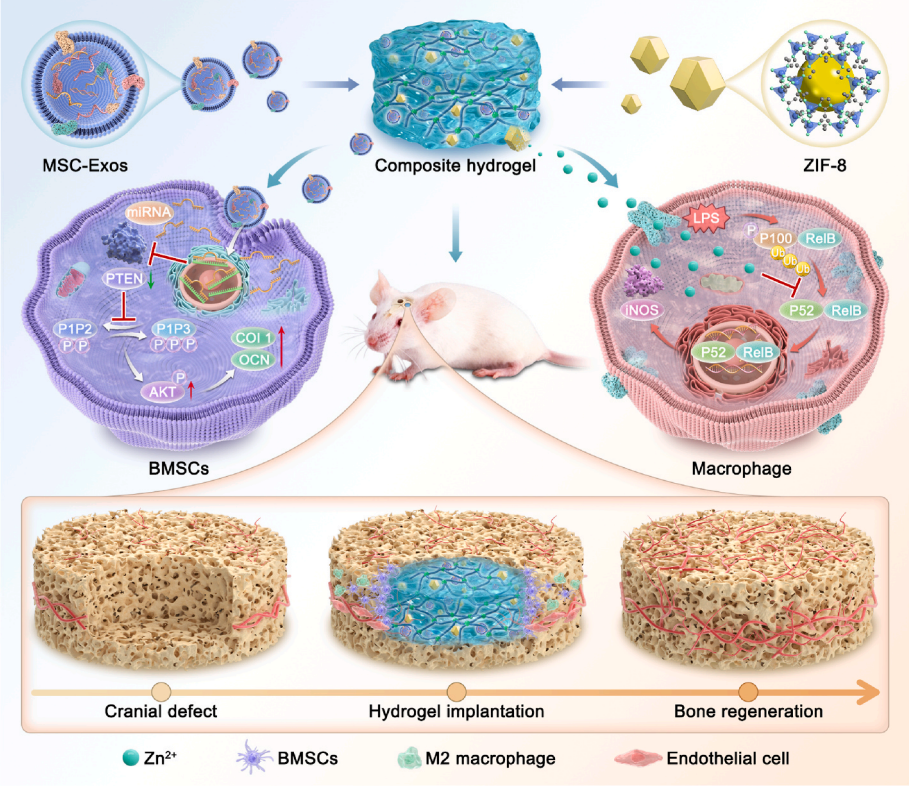

Scheme 1. Schematic illustration of the composite hydrogel scaffold for synergistic therapy of bone defects.

droplet accumulation, and chondrogenic differentiation was assessed by Alcian Blue staining to visualize glycosaminoglycan deposition (Fig. S1).

2.2. Isolation of MSC-Exos

MSC-Exos with osteoinductive effects were isolated from osteogenically pre-differentiated BMSCs by means of ultracentrifugation. Specifically, when BMSCs (passage 3) achieved a confluence of 70 %, the basic medium was replaced with an osteogenic induction medium (OIM) for pre-differentiation. The OIM is composed of α-MEM, 0.1 μM dexamethasone, 50 μM L-ascorbic acid, and 10 mM sodium β-glycerophosphate. The OIM was refreshed every two days. After two weeks of osteogenic induction, the exosomes secreted by BMSCs exhibited optimal osteogenic induction activity [28]. The OIM was replaced with a basic medium supplied with 10 % exosome-depleted FBS. The medium supernatant was collected after 48 h of incubation and subjected to subsequent ultracentrifugation. In order to prevent potential exosome degradation, all centrifugation procedures were set to be conducted at 4 °C. To eliminate suspended and dead cells, the supernatant was successively centrifuged at 500×*g* and 3000×*g* for 10 min each time. Subsequently, the collected supernatant was centrifuged at a speed of 10,000×*g* for 30 min in order to separate and discard the cell debris effectively. The supernatant was then filtered using a 0.22 μm PES filter, which guaranteed the successful removal of microvesicles. After filtration, the supernatant was centrifuged at 100,000×*g* for 1.5 h with a Beckman Coulter 70i rotor (Beckman Coulter, Fullerton, CA) to collect the pristine exosomal extract. The resulting exosome pellet was rinsed with PBS. Finally, it was ultracentrifuged again at 100,000×*g* for 90 min to obtain purified exosomes.

2.3. Synthesis of ZIF-8

The synthetic route of ZIF-8 nanoparticles followes the previous work [46]. With a mole ratio of 1:8, $Zn(NO_3)\cdot 6H_2O$ and 2-methylimidazole were fully dissolved in methanol and stirred at 600 rpm for 1 h, resulting in the formation of milky white precipitates of the initial ZIF-8 nanoparticles. The mixture underwent centrifugation at 9000 rpm for 20 min, followed by three washes with methanol and ultrapure water. The final ZIF-8 nanoparticles were then obtained through vacuum drying.

2.4. Preparation of composite hydrogels

For GelMA hydrogel preparation, the combination of 90 % amino substitution degree GelMA and 10 % w/v concentration (GM90-10 %) was selected for its optimal mechanical properties, biocompatibility, and photocrosslinking efficiency, which has become the mainstream choice for tissue engineering, 3D printing, and cell culture [47,48]. The fabrication of the GelMA hydrogel involved dissolving 10 % (w/v) GelMA in ultrapure water at 50 °C, followed by vigorous stirring until a transparent solution was obtained. Afterward, 0.5 % (w/v) LAP was added to the GelMA solution. The prepolymer solution was transferred into the cell culture well plate and then irradiated with UV light (405 nm, 30 W) for 1 min, thereby obtaining the GelMA hydrogel. The same approach was employed to produce MSC-Exos/ZIF-8 incorporated hydrogels. ZIF-8 nanoparticles were ultrasonically dispersed in the GelMA prepolymer solution, and subsequently, MSC-Exos (1×10^{10} particles/mL) were introduced into the mixed solution and homogeneously mixed in a vortex oscillator. The exosome concentration in the hydrogel refers to the effective dosages reported in previous studies [28,49]. The loading amount of ZIF-8 nanoparticles in GelMA hydrogels is determined based on the biocompatibility and osteogenic properties. As shown in Fig. S2, when the concentration of ZIF-8 in the GelMA prepolymer solution is 20 mg/mL, the resultant hydrogel exhibits excellent cell compatibility and optimal osteogenic properties. The encapsulation concentration of exosomes in hydrogels was based on previous reports. In this study, the pure GelMA hydrogel, hydrogel encapsulated with ZIF-8, hydrogel encapsulated with MSC-Exos, and hydrogel

encapsulated with both ZIF-8 and MSC-Exos were respectively assigned as Gel, ZIF-8@Gel, Exo@Gel, and Z/E@Gel.

2.5. Characterization of composite hydrogels

The characterization of GelMA was performed using ^{1}H NMR (Advance AV500 MHz, Bruker, Switzerland). The chemical composition of hydrogels was investigated by FTIR (IRAffinity-1S, Shimadzu, Japan). Confocal laser scanning microscopy (Stellaris, Leica, Germany) was employed to analyze the distribution of exosomes labeled with PKH67 within the hydrogels. SEM (Gemini 500, Zeiss, Germany) was applied to examine the cross-sectional morphology of the samples. The mechanical characteristics of the hydrogels were assessed by evaluating the compression performance of cylindrical specimens (diameter: 10 mm, height: 4 mm) using an electronic universal testing machine (68SC-2, Instron, USA) at a compression rate of 2 mm/min and room temperature. The compression modulus was measured within the 0–10 % linear strain range.

2.6. Exosome labeling and uptake assay

The isolated exosomes were marked with the PKH67 Green Fluorescent Cell Linking Kit (Beijing Fluorescence Biotechnology, China). Specifically, 20 μg of the MSC-Exos were combined with 1 mL of Diluent C for General Membrane Labeling, followed by the addition of 2 μL of PKH67 dye. In an effort to mitigate non-specific binding, 2.5 mL of 0.5 % BSA was incorporated into the reaction buffer. Subsequently, the labeled exosomes were dispersed in 5 mL of PBS and subsequently underwent ultracentrifugation at 100,000×*g* for 60 min to eliminate the unlabeled dye. The PKH67-labeled MSC-Exos were then encapsulated within the GelMA hydrogel, following the procedure outlined in Section 2.4. The cells were then incubated with the hydrogel loaded with the labeled exosomes in a basic medium for 12 h. Finally, the cells were treated with 4 % paraformaldehyde (PFA) for 30 min and incubated with FITC-phalloidin (Beyotime, China) and DAPI (Servicebio, China) in the dark for 15 min. The endocytosis of the MSC-Exos was visualized using CLSM.

2.7. Cell viability assay

BMSCs were seeded into 96-well plates covered with hydrogel at a density of 1×10^5 cells/well and cultured in 100 μL of growth medium. After 1, 3, and 5 days of culture, the original medium was replaced with 100 μL of fresh medium containing 10 μL of CCK-8 solution. The cells were then cultured in a cell culture incubator for 2 h. The absorbance values (OD values) were recorded at 450 nm with a microplate reader (BioTek, USA).

2.8. ALP activity and staining assay

BMSCs were seeded into 24-well plates with a 2×10^5 cells/well density. The ALP activity of BMSCs incubated with hydrogels was evaluated after 4 and 7 days of osteogenic induction. Osteoblasts were harvested, lysed with 1 % Triton X-100 for 30 min, and then centrifuged at 12,000 rpm for 5 min to collect the supernatant. The measurement of total intracellular protein was conducted with a BCA protein assay kit, and the evaluation of ALP expression utilized a p-nitrophenyl phosphate assay kit (Yeasen, China). ALP activities were calibrated according to the complete protein content detected in the cells. For ALP staining, osteoblasts were treated with 4 % PFA for fixation and then stained utilizing an ALP staining kit (Applygen, China). After rinsing with PBS, the specimens were photographed and analyzed under a stereomicroscope (MZ10 F, Leica, Germany).

2.9. Alizarin Red S staining

BMSCs were introduced into 24-well plates with a density of 2×10^5 cells for each well. After two weeks of osteogenic induction, the mineralization status of the extracellular matrix was analyzed using Alizarin Red S (ARS, Beyotime, China) staining. The osteoblasts were fixed using 4 % PFA and incubated with a 40 mM ARS solution in Tris-HCl buffer (pH 4.1) for 1 h. After rinsing with ultrapure water, the specimens were photographed with a stereomicroscope (MZ10 F, Leica, Germany).

2.10. Flow cytometry

RAW264.7 cells were treated with LPS (100 ng/mL) for 24 h to simulate the inflammatory response and then incubated with different samples until an appropriate density was achieved. Subsequently, the cells were harvested, washed with PBS, and resuspended in a medium containing 1 % BSA to block non-specific binding sites. The cells were then divided into two groups, and fluorescently labeled antibodies against FITC anti-mouse F4/80 (BioLegend, USA), APC anti-mouse CCR7 (BioLegend, USA), and PE anti-mouse CD206 (BioLegend, USA) were added to each group, while corresponding isotype controls were established. The cells were treated with the antibodies, avoiding light at 4 °C for 2 h, and subsequently, PBS was utilized to eliminate any unbound antibodies. Finally, the expression levels of CCR7 and CD206 were analyzed using a CytoFLEX flow cytometer (Beckman, USA) and evaluated via FlowJo software (TreeStar, USA).

2.11. Immunofluorescence staining

Following a 14-day osteogenic induction period, immunofluorescence staining was conducted on BMSCs to evaluate the expression of OCN and Col I proteins. Additionally, immunofluorescence staining was performed to evaluate the expression of iNOS, CD206, and CD86 in RAW264.7 cells under simulated inflammatory conditions. Specifically, the cells were fixed with 4 % PFA for half an hour in 24-well plates. They were then permeabilized using 0.1 % Triton X-100 for 30 min and blocked with goat serum (Servicebio, China) for 30 min to reduce non-specific binding. Primary antibodies were added and incubated overnight at 4 °C, followed by incubation with the corresponding secondary antibodies in the dark at room temperature for 2 h. The cells were subsequently rinsed, and DAPI was applied for nuclear staining. The cells were incubated at room temperature for 15 min. After another rinse, the samples were prepared for CLSM imaging.

2.12. Evaluation of the migratory capacity of HUVECs

The migratory capacity of HUVECs was evaluated through a line scratch model. HUVECs were inoculated into 12-well plates at a density of 2×10^5 cells per well. During the cell culture process, it was ensured that the cells could grow well in the culture medium containing the hydrogel extract and form a monolayer. When the confluence of the monolayer reached approximately 95 %, a specific tool was employed to create a linear scratch on the monolayer. After creating the scratch, the HUVECs were cultured in serum-free medium for continued incubation. The migration of HUVECs in the scratch area was captured by a phase-contrast microscope (Zeiss, Germany), allowing for quantitative analysis of the migratory capacity.

2.13. Tube formation assay

The tubular structure formation capability of HUVECs was assessed using Matrigel (BD Biosciences, USA). To ensure complete melting, the Matrigel was thawed overnight on ice. Following this, 300 μL of Matrigel was dispensed onto the surface of a 24-well plate and incubated at 37 °C in a cell culture incubator for 30 min to allow solidification. Once the Matrigel had solidified, pre-treated HUVECs were seeded onto it at a density of 2×10^4 cells per well and cultured for 24 h. The morphology and number of tubular structures formed by HUVECs on the Matrigel

were examined using a stereomicroscope.

2.14. Western blot analysis

Cells were inoculated into 6-well plates. At predetermined time points, cells were washed three times with PBS, followed by the addition of 1 mL of lysis buffer containing protease inhibitors, phosphatase inhibitors, and phenylmethylsulfonyl fluoride for cell lysis. The lysate was mixed with the loading buffer in a ratio of 1:4 and boiled in boiling water for 10 min to achieve protein denaturation. The protein samples were loaded onto the lanes of a polyacrylamide gel for SDS-PAGE separation at room temperature. The proteins were then transferred to a PVDF membrane. At room temperature, the PVDF membrane was blocked with 5 % skimmed milk for 2 h and then incubated with primary antibodies overnight at 4 °C. After three washes with TBST, the membrane was incubated with HRP-conjugated secondary antibodies for 2 h at room temperature. Protein bands were detected using Super ECL Plus luminous solution (Applygen, China), and band intensities were quantitatively analyzed using Image J software (NIH, USA).

2.15. RNA sequencing

RAW264.7 cells were inoculated into 6-well plates at a density of 1×10^5 cells per well on hydrogels, and RNA was subsequently extracted using Trizol Reagent (Vazyme, China). Whole-genome sequencing was conducted on the NovaSeq 6000 platform (Illumina, USA) by the Beijing Genomics Institute (China), yielding approximately 20 million 150 bp paired-end reads per sample. Low-quality reads and adapter sequences were removed using Trimmomatic, and quality control was performed with FastQC. Differential gene expression analysis was carried out using the DESeq2 R package, while KOBAS software was employed for KEGG pathway enrichment analysis to elucidate gene functions. Differentially expressed genes were identified based on a p-value threshold of <0.05, with multiple comparison corrections applied to calculate q-values, setting the significance level at q-value <0.05.

2.16. Mirco-RNA transfection

BMSCs were inoculated into suitable culture dishes and maintained until they reached 70 % confluence. The miRNA mimics and inhibitors were obtained from Guangzhou RiboBio Co., Ltd. To prepare the transfection complexes, miRNA mimics or inhibitors were mixed with Lipofectamine RNAiMAX transfection reagent (Invitrogen, USA) in Opti-MEM reduced-serum medium and incubated at room temperature for 10 min. These complexes were then added to the BMSCs and incubated at 37 °C for 8 h. Following this, the medium was replaced with fresh basic medium, and the cells were incubated for an additional 24 h. The transfected BMSCs were subsequently harvested for subsequent osteogenic induction experiments.

2.17. In vivo implantation of hydrogels

All animal procedures were approved by the Shenzhen Institute for Drug Control (approval number 20240528). All *in vivo* experiments were conducted in compliance with the Animal Research: Reporting of In Vivo Experiments (ARRIVE) 2.0 guidelines. In this study, 8-week-old male SD rats weighing approximately 200 g were used to assess the *in vivo* bone-inducing capability of the hydrogel. The rats were raised in a standard animal facility maintained at a constant temperature of 22 °C. Anesthesia was initiated by administering 50 mg/kg of 10 % pentobarbital sodium via an intraperitoneal injection. Iodophor was employed to sterilize the shaved cranial area. A 1.5-cm incision was executed longitudinally along the midline of the skull, which exposed the sagittal suture, the parietal bones bilaterally, and areas of the frontal and occipital bones. The parietal periosteum was then longitudinally incised and carefully dissected using blunt dissection techniques. A cranial drill was employed to generate circular bone defects, each around 5 mm in diameter, on both the left and right parietal bones. Normal saline was applied during drilling for cooling purposes, and appropriately sized hydrogels were implanted into the defect sites. The periosteum and skin were subsequently closed with surgical sutures. Following the operation, a three-day course of penicillin was given to avert the possibility of infection.

2.18. Micro-CT scanning

Following the implantation surgery, all rats underwent euthanasia via CO_2 inhalation in the eighth week. The cranial bones were collected and stored in 4 % PFA at 4 °C. Subsequently, micro-computed tomography (NMC-200, NEMO) was performed on the samples using an X-ray tube set at 70 kV and 60 μA, with data acquisition conducted using Cruiser software. After scanning, the raw data were reconstructed using Recon software to generate three-dimensional images. Bone regeneration at the cranial defect sites was analyzed using Avatar software.

2.19. Blood biochemical tests

To evaluate hepatic and renal injury, whole blood was collected from SD rats 4 weeks post-implantation of the hydrogel scaffold and allowed to stand at room temperature for 2 h to separate serum samples. At 1 and 4 weeks post-implantation, whole blood was collected via cardiac puncture from rats, and serum zinc ion concentrations were measured. The blood was then centrifuged at 3000 g for 15 min, and the supernatant was collected and stored at −80 °C. Serum levels of zinc ion, aspartate aminotransferase (AST), alanine aminotransferase (ALT), total bilirubin (TBIL), blood urea nitrogen (BUN), creatinine (CREA), and uric acid (UA) were measured by Wuhan Servicebio Technology Co., Ltd. (Wuhan, China) using a Chemray 240 automatic biochemical analyzer (Shenzhen, Rituo Technology).

2.20. Histological and immunofluorescence staining

Rat cranial samples were subjected to fixation in a 10 % neutral buffered formalin for a total of 48 h. A 10 % EDTA solution was employed for decalcifying the samples, with pH levels regulated to between 7.2 and 7.4, and they were subsequently stored at a temperature of 4 °C. After one month of decalcification, the samples underwent gradient alcohol dehydration and xylene hyalinization. Subsequently, the samples were embedded in molten paraffin and sectioned into 5–10 μm thick slices using a microtome. The slices were mounted on glass slides and baked in an oven at 60 °C for 30 min to ensure proper adhesion. Then, the slices were dewaxed and rehydrated with xylene and gradient alcohols. Histological evaluation of bone defect regeneration following hydrogel implantation was conducted using hematoxylin and eosin (H&E) staining and Masson's trichrome staining. For immunofluorescence staining, paraffin sections were subjected to antigen retrieval using an EDTA antigen repair solution, followed by blocking with an antigen-blocking solution to reduce non-specific background staining.

2.21. Statistical analysis

The statistical analysis presents the mean and standard deviation, ensuring that three or six distinct replicates represent each biological sample. The statistical significance of variations among multiple groups was determined using a one-way analysis of variance. Statistical analyses were conducted through GraphPad Prism 9 software (San Diego, USA). A p-value less than 0.05 was considered statistically significant.

3. Results and discussion

3.1. Characterization of ZIF-8 and MSC-Exos

ZIF-8 nanoparticles were fabricated based on a facile one-pot synthetic route, as depicted in Fig. 1(A). Zn^{2+} and 2-methylimidazole form ZIF-8 through a self-assembly process in methanol solvent. Specifically, the Zn^{2+} interacts with the nitrogen atom of 2-methylimidazole (2-MIM) via a coordination bond to form a tetrahedral structural unit of Zn(2-MIM)$_4$. As the coordination reaction progresses, the Zn(2-MIM)$_4$ structural units aggregate, forming the primary nucleus. Once the nuclei are formed, additional Zn(2-MIM)$_4$ units attach to the nuclei through coordination bonds, facilitating the growth of the crystal until a stable ZIF-8 topological structure is established. Fig. 1(B) illustrates that the bone-functionalized MSC-Exos were isolated from osteogenic pre-differentiated BMSCs by ultracentrifugation. According to a previous report, BMSCs in osteogenic induction culture conditions were able to significantly enhance the osteoinductive properties of their secreted MSC-Exos through the modulation of multicomponent miRNAs [49]. At the same time, another study indicated that BMSCs pre-differentiated for 10–15 days could generate MSC-Exos with optimal osteogenic activity [28]. Consequently, in this study, MSC-Exos were collected from the supernatant of BMSCs culture medium following 14 days of osteogenic induction.

The morphology and elemental composition of the fabricated ZIF-8 nanoparticles were characterized by TEM and EDS and depicted in Fig. 1(C). ZIF-8 nanoparticles display a distinct rhombic dodecahedral structure, measuring approximately 400 nm in average size, while the elements Zn, C, N, and O are evenly dispersed within the material. Previous research has indicated that nanoscale ZIF-8 possesses excellent biocompatibility, whereas micrometer-scale ZIF-8 demonstrates significant cytotoxicity [50]. The disparity in biocompatibility between nanoscale and micro-scale ZIF-8 remains undefined to date. Existing studies reveal that BMSCs internalize ZIF-8 nanoparticles via caveolin-mediated endocytosis and phagocytosis [51]. Efficient uptake of ZIF-8 nanoparticles in BMSCs was similarly observed in Fig. 1(D) and enhanced with increasing ZIF-8 concentration. The exposure of BMSCs to ZIF-8 nanoparticles at a concentration of 100 μg/mL for 24 h resulted in no notable changes in the number or morphology of the cells, demonstrating the outstanding biocompatibility of the synthesized ZIF-8 nanoparticles.

The morphology and size distribution of MSC-Exos were confirmed

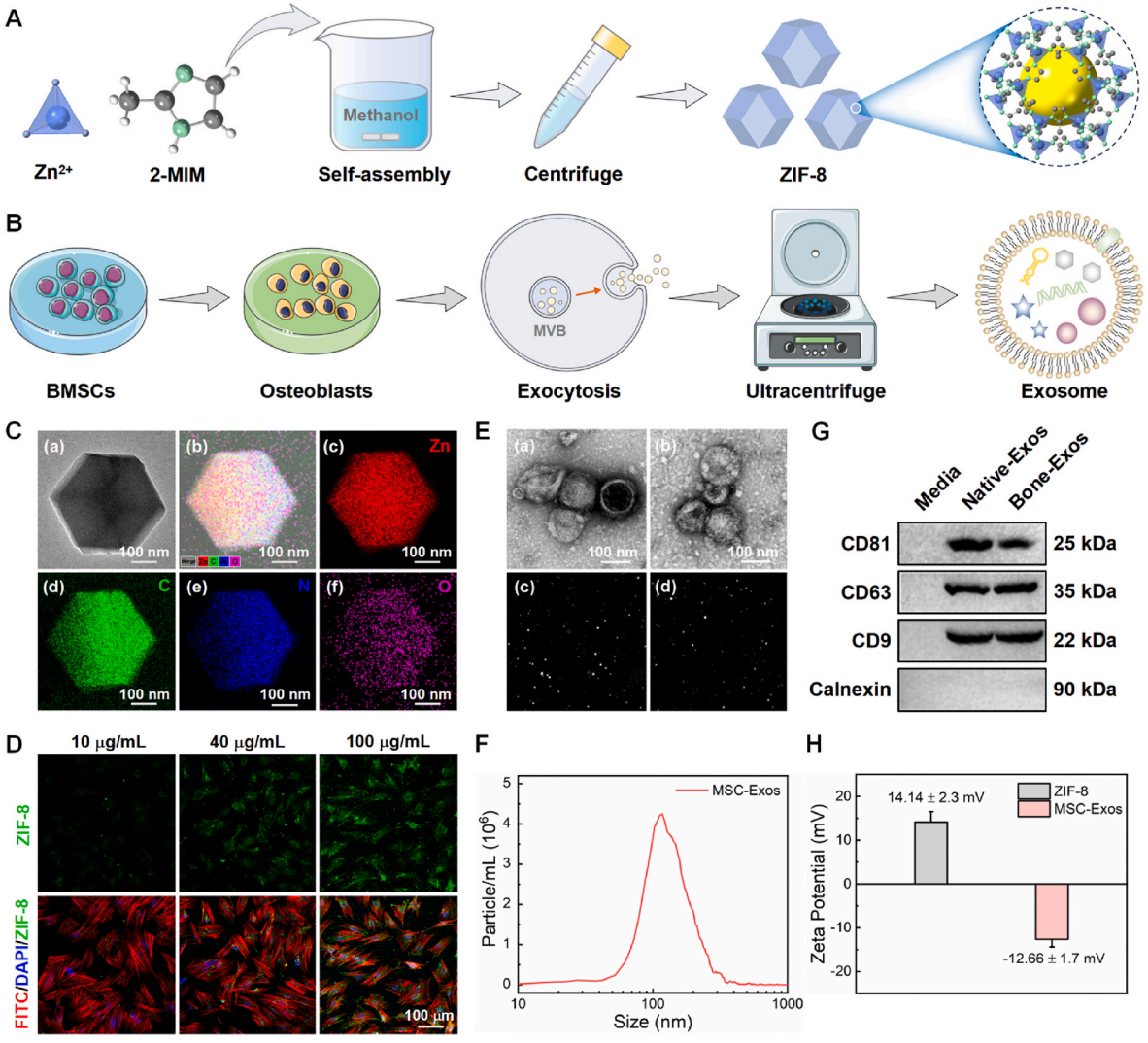

Fig. 1. Fabrication of ZIF-8 nanoparticles and isolation of MSC-Exos. (A) The preparation route of ZIF-8 nanoparticles. (B) Isolation procedure of MSC-Exos from osteogenically pre-differentiated BMSCs. (C) TEM image (a) and element distribution images (b–f) of ZIF-8 nanoparticle. (D) Morphological observation of BMSCs incubated with different concentrations of ZIF-8 nanoparticles. (E) TEM images and video tracking snapshots of native MSC-Exos (a, c) and bone-functionalized MSC-Exos (b, d). (F) NTA of the bone-functionalized MSC-Exos. (G) Western blotting of surface markers of the bone-functionalized MSC-Exos. (H) Evaluation of Zeta potential.

via TEM and NTA, as depicted in Fig. 1(E and F). Osteogenic induction of BMSCs did not alter the morphology of their secreted exosomes, and both exosomes presented a spherical or slightly oval profile. As intracellular nanovesicles, exosome release is initiated by the fusion of multivesicular bodies (MVBs) with cell membranes, resulting in the absence of discernible organelles within these particles [12]. The NTA analysis indicated that the average particle diameter of MSC-Exos was 157.2 nm, and the size distribution ranged from 40 to 200 nm, which was close to the typical particle size of exosomes. Moreover, western blotting confirmed the expression of exosomal marker proteins such as CD63, CD9, and CD81 in MSC-Exos, while the typical endoplasmic reticulum molecular chaperone protein Calnexin was absent (Fig. 1(G)). Based on the foregoing analysis, the highly pure exosomes were successfully obtained through ultracentrifugation, and the existence of cell debris and microvesicles was ruled out.

Exosomes are derived from the endosomal system of cells, encapsulating specific components of the source cells without containing intact organelles such as nuclei, mitochondria, or endoplasmic reticulum [52]. The cell nucleus, housing the complete set of genetic material, represents one of the primary sources triggering immune rejection associated with implanted cells. Owing to the absence of nuclei, MSC-Exos do not express donor-derived intact MHC-I/II molecules, leading to a significant reduction in immunogenicity [53]. When applied to bone tissue engineering scaffolds, MSC-Exos effectively circumvent the risk of immune rejection induced by implanted intact allogeneic cells [54], while transmitting key bone repair signals to promote host-mediated bone regeneration, thus representing a promising therapeutic strategy for bone tissue regeneration.

Additionally, the Zeta potentials of ZIF-8 and MSC-Exos in PBS were measured to be 14.14 mV and −12.66 mV, respectively (Fig. 1(H)). The Zeta potential of nanoparticles is associated with their surface charge. Since cell membranes typically bear negative charges, exosomes also present a negative charge [55]. Generally, cationic nanoparticles exhibit cytotoxicity related to membrane disruption. In this study, the negative potential of MSC-Exos can neutralize the positive potential of ZIF-8 nanoparticles, thereby reducing the cytotoxicity. Simultaneously, the positively charged ZIF-8 can also delay the release of MSC-Exos via electrostatic interactions.

Detailed material characterization was conducted following the preparation of ZIF-8 nanoparticles to provide insight into their biological function in composite hydrogels. The well-defined and intense diffraction peaks at 2θ values of 7.35°, 10.40°, 12.75°, 14.73°, 16.48°, 18.07°, 22.17°, 24.55°, and 26.73° in Fig. 2(A) indicate that the ZIF-8 nanoparticles exhibit a highly crystalline rhombohedral structure. These peaks correspond to the (011), (002), (112), (022), (013), (222), (114), (233), and (134) crystal planes, respectively. Meanwhile, the crystal structure of the ZIF-8 nanoparticles is in good accordance with the simulated ZIF-8, suggesting its high purity. The ZIF-8 nanoparticles

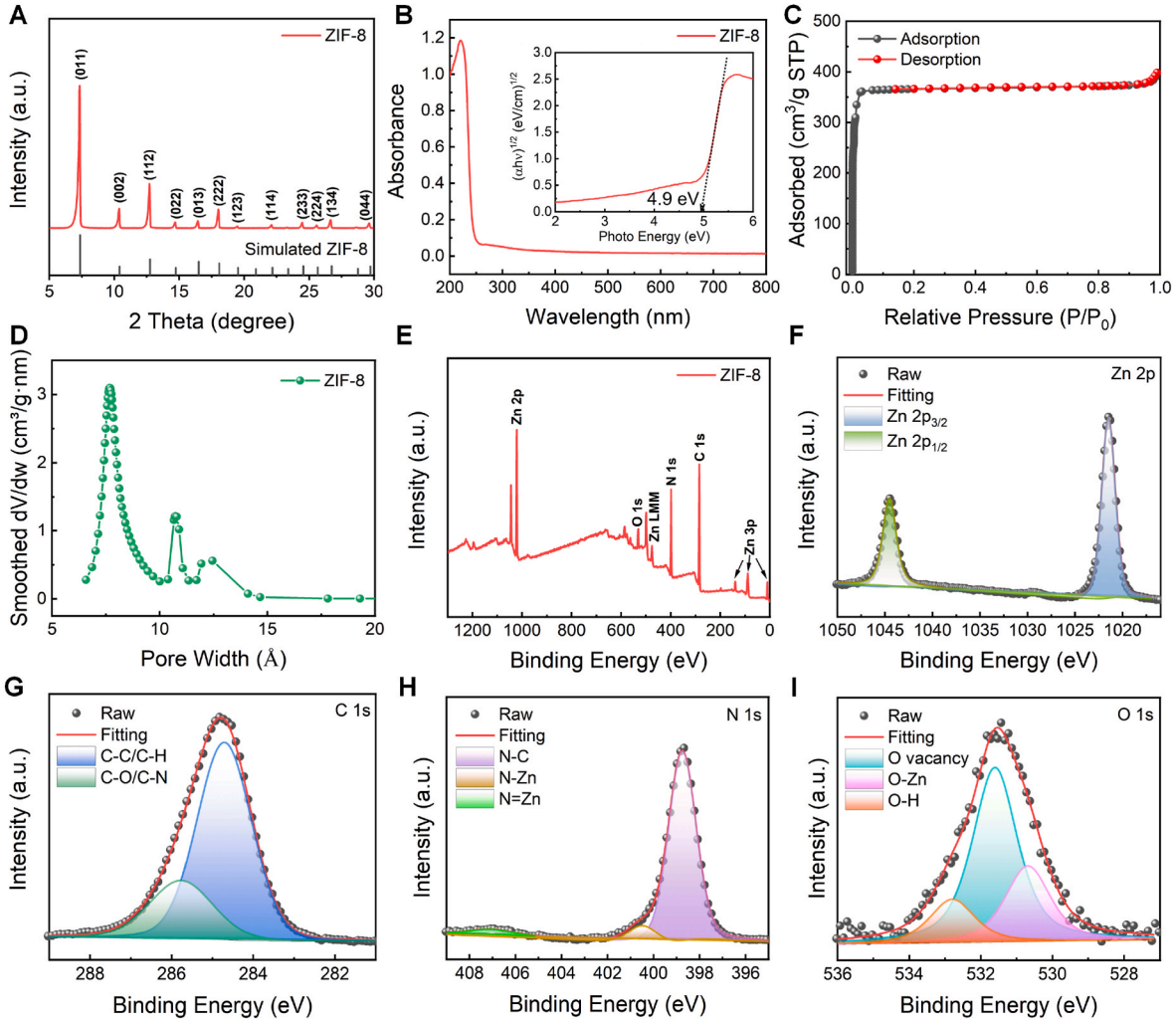

Fig. 2. Characterization of the ZIF-8 nanoparticles. (A) XRD spectra of the ZIF-8 nanoparticles. (B) UV–visible absorption spectra of the ZIF-8 nanoparticles, the inset is the Tauc plot of ZIF-8. (C) Nitrogen adsorption-desorption isotherm of the ZIF-8 nanoparticles. (D) Pore diameter distribution of the ZIF-8 nanoparticles. (E) XPS survey spectra of the ZIF-8 nanoparticles. (F–I) High-resolution XPS spectra of Zn 2p, C 1s, N 1s, and O 1s of the ZIF-8 nanoparticles.

demonstrate a strong light absorption within the narrow ultraviolet range of 200–230 nm, yet exhibit nearly no absorption within the visible light range (Fig. 2(B)). A Tauc plot was employed to calculate the optical band-gap of ZIF-8, and is illustrated in the inset of Fig. 2(B). The absorption cut-off edge of ZIF-8 is approximately 253 nm, corresponding to an optical band gap of 4.9 eV. The wide band gap of ZIF-8 restricts the response to visible light. Therefore, no active free radicals are generated under 405 nm blue-violet light irradiation, and the inherent photocrosslinking mechanism of the GelMA hydrogel remains unchanged. As illustrated in Fig. 2(C), the ZIF-8 nanoparticles manifest a Type I isotherm. The nitrogen adsorption rises rapidly at relatively low pressures and reaches saturation at a certain relative pressure. ZIF-8 nanoparticles demonstrate a high specific surface area, and the Brunauer-Emmett-Teller (BET) specific surface area is calculated as 1154.89 m^2/g. From the Horvath-Kawazoe differential pore volume plot in Fig. 2(D), it is observed that the pore diameter of ZIF-8 nanoparticles falls within the range of 0.6–1.5 nm, which can be classified as micropores (less than 2 nm). The nanoscale pore structure of ZIF-8 is beneficial for the sustained and gradual release of encapsulated zinc ions.

The XPS survey spectra reveal that ZIF-8 is primarily composed of Zn, C, N, and O elements, consistent with the EDS results, as illustrated in Fig. 2(E). Among them, Zn is an essential trace element and is of vital importance for enzymatic reactions and protein functions within the body. Meanwhile, C, N, and O are fundamental elements constituting the organic and inorganic components of the human body. In the Zn 2p spectra of ZIF-8, the double peaks at 1021.5 eV and 1044.7 eV are attributed to Zn $2p_{3/2}$ and Zn $2p_{1/2}$, as depicted in Fig. 2(F). The spin-orbit splitting energy of Zn 2p amounts to 23.2 eV, suggesting that the zinc element in ZIF-8 exists in the form of Zn^{2+}. In the C 1s spectra (Fig. 2(G)), the peaks located at 284.8 eV and 285.8 eV are attributed to C-C/C-H and C-O/C-N, respectively. The main peak of N 1s at 398.8 eV is attributed to N-C, while the peaks at 400.5 eV and 407.1 eV are attributed to N-Zn and N=Zn, respectively (Fig. 2(H)). The O 1s spectra can be deconvoluted into three sub-peaks at 530.6 eV, 531.8 eV, and 532.8 eV, which are attributed to O-Zn, O vacancies, and O-H bonds, respectively (Fig. 2(I)).

3.2. Characterization of composite hydrogel

GelMA, a widely utilized hydrogel material, features a three-dimensional architecture that facilitates cell growth and differentiation [56]. The internal three-dimensional network structure of the GelMA hydrogel provides ample space for exosome loading, effectively maintains exosome activity, and has been extensively utilized to construct exosome delivery systems [57]. In this study, MSC-Exos and ZIF-8 nanoparticles were concurrently encapsulated in the GelMA

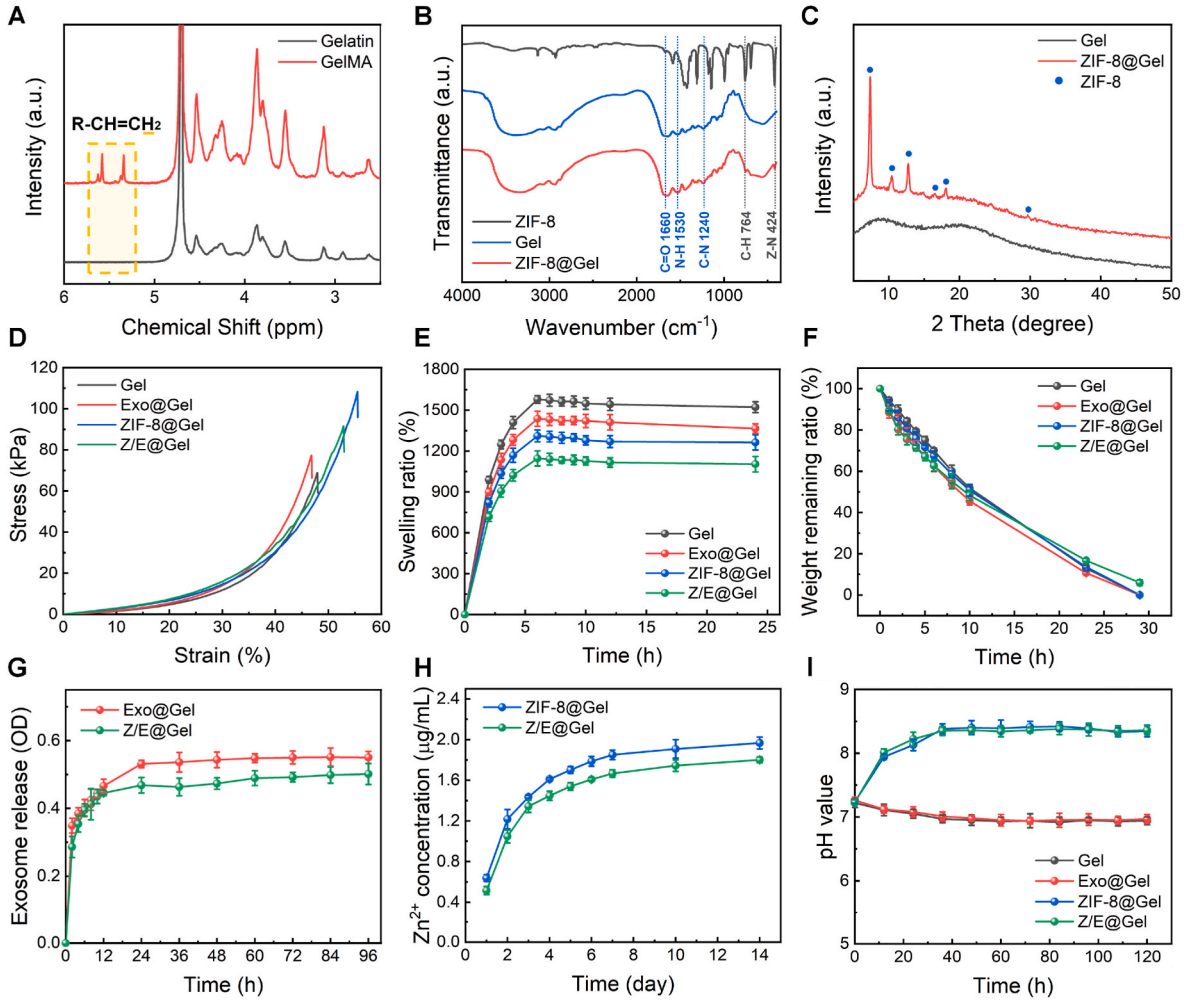

Fig. 3. Characterization of MSC-Exos and ZIF-8 encapsulated GelMA hydrogels. (A) ^{1}H NMR spectrum of the gelatin and GelMA. (B) FTIR spectroscopy of the composite hydrogels. (C) XRD spectra of Gel and ZIF-8@Gel. (D) Strain-stress curves of the hydrogels in compression testing. (E) Swelling property of the hydrogels in PBS. (F) Degradation of the hydrogels in PBS containing 5 U/mL type II collagenase. (G) Release profiles of exosomes in the MSC-Exos encapsulated hydrogels. (H) Cumulative concentration of Zn^{2+} released from hydrogels immersed in PBS. (I) The pH values of PBS after hydrogel immersion. All data are presented as the mean ± SD (n = 3).

hydrogel, with the anticipation of constructing a composite hydrogel featuring synergistic osteogenesis and immunomodulation. During the synthesis of GelMA, gelatin undergoes modification through the introduction of methacrylic acid (MA), substituting some amino groups in gelatin with methacrylate groups [58]. The bioactivity and thermal stability of GelMA have both been enhanced compared to those of gelatin. The local structure of the GelMA molecule was identified by ^{1}H NMR (Fig. 3(A)). Following modification with MA, the peak intensity associated with the lysine methylene protons at 2.93 ppm in gelatin was markedly reduced. Additionally, the presence of alkenyl groups (R-CH=CH_2) in GelMA was confirmed by the detection of two absorption peaks at 5.34 ppm and 5.57 ppm [59]. These findings confirm that MA was successfully grafted onto gelatin, with the degree of substitution calculated at 89 %. As presented in Fig. 3(B), the infrared spectrum exhibits characteristic absorption peaks of gelatin at three distinct regions: the amide I band at 1660 cm^{-1} (attributed to C=O stretching vibration), the amide II band at 1530 cm^{-1} (corresponding to N-H bending and C-N stretching vibrations), and the amide III band at 1240 cm^{-1} (indicative of C-N stretching and N-H bending vibrations) [60]. Meanwhile, the vibrational peaks of Zn-N coordination bond (424 cm^{-1}) and the vibrational peak of C-H out-of-plane bending on the 2-methylimidazole ring (764 cm^{-1}) in ZIF-8 could be observed in the infrared spectra of ZIF-8@Gel, whereas they were not observed in Gel, which further proves the successful preparation of the ZIF-8@Gel composite hydrogel [61]. The phase structure of ZIF-8@Gel was characterized through XRD (Fig. 3(C)). The characteristic diffraction peaks attributed to ZIF-8 can be clearly observed in the XRD pattern of ZIF-8@Gel, demonstrating that ZIF-8 can still maintain a good crystal structure in GelMA hydrogel.

The effects of the introduction of MSC-Exos and ZIF-8 on the mechanical performance of GelMA hydrogels were also analyzed (Fig. 3 (D)). The compression test indicated that the incorporation of ZIF-8 was capable of reinforcing the mechanical strength of GelMA hydrogels. The compression strength rose from 68.8 ± 4.2 kPa for Gel to 108.3 ± 7.1 kPa for ZIF-8@Gel, and the compression modulus also increased from 15.2 ± 1.3 kPa for Gel to 26.7 ± 2.5 kPa for ZIF-8@Gel (Fig. S3). By contrast, the introduction of MSC-Exos exerted a relatively minor influence on the mechanical strength of GelMA hydrogel. Apart from mechanical properties, swelling and degradation behaviors are also crucial when applying bone graft materials. As shown in Fig. 3(E), all the hydrogels swelled rapidly within 6 h and reached equilibrium within 10 h. The introduction of MSC-Exos and ZIF-8 decreased the equilibrium swelling ratio of GelMA hydrogels. The equilibrium swelling ratio of Z/E@Gel decreased from 1521 ± 39 % of Gel to 1103 ± 56 %. The decreased swelling ratio will enhance the mechanical strength and stability of the hydrogels and alleviate the compression on the surrounding tissues. Furthermore, all the hydrogels exhibited excellent biodegradability in the PBS solution containing 5 U/mL type II collagenase at 37 °C (Fig. 3(F)). The incorporation of MSC-Exos and ZIF-8 did not significantly impact the degradation profile of the GelMA hydrogels, with all hydrogels exhibiting near-complete degradation after approximately 30 h.

The porous structure of the GelMA hydrogel facilitates the sustained release of encapsulated bioactive components, thereby promoting bone tissue regeneration. As seen in Fig. 3(G), the exosomes in Exo@Gel and Z/E@Gel were released rapidly within 12 h, followed by a sustained and slow release profile. Notably, the exosome release rate of Z/E@Gel is significantly slower than that of Exo@Gel, which facilitates a more sustained and effective exosome-based therapy. The release behavior of zinc ions within the hydrogels was also assessed, as presented in Fig. 3 (H). The two ZIF-8-containing hydrogels exhibited a relatively high rate of zinc ion release during the initial three days, followed by a plateau in the release rate. Consistent with the exosome release behavior, the zinc ion release rate in Z/E@Gel was slightly lower compared to that in ZIF-8@Gel. It can be hypothesized that the MSC-Exos and ZIF-8 with opposite Zeta potentials within the hydrogel could retard the release of exosomes and the degradation of ZIF-8 via electrostatic interactions. In physiological conditions, the extracellular pH is crucial for regulating bone formation and resorption [62]. Osteogenesis-related ALP activity and bone collagen deposition are typically suppressed under acidic conditions. Meanwhile, in alkaline conditions, the mineralization of osteoblasts is enhanced, thereby facilitating bone regeneration [35]. Furthermore, an alkaline environment can also effectively modulate over-activated osteoclast activity, thereby suppressing bone resorption [63]. Nevertheless, extremely acidic and alkaline environments beyond the rational pH range (6.5–10.5) can also reduce cell activity and impair proliferation [64]. Therefore, the pH in the supernatant of PBS soaked with hydrogel was recorded and presented in Fig. 3(I). The pH value of the hydrogels incorporating ZIF-8 stabilized at approximately 8.3 after 48 h of immersion, whereas the introduction of exosomes exerted nearly no influence on the pH. The ZIF-8-encapsulated hydrogel demonstrates significant potential to accelerate bone regeneration by establishing a mildly alkaline microenvironment that is conducive to osteogenesis.

3.3. Biocompatibility assessment in vitro

As depicted in Fig. 4(A), GelMA is synthesized through the modification of gelatin by MA. Subsequently, the MSC-Exos and ZIF-8 nanoparticles of appropriate concentrations were uniformly dispersed in the GelMA prepolymer solution, and the photo-crosslinking gelation was initiated with LAP as the photoinitiator under 405 nm light irradiation. The excited state of LAP will decompose and generate free radicals, which react with the methacrylate groups in GelMA molecules to trigger the cross-linking reaction [65]. GelMA molecules are connected through cross-linking reactions to generate a three-dimensional network structure of hydrogels. The cross-sectional SEM images of the hydrogels in Fig. 4(B) show that all the hydrogels present highly interconnected and porous structures identical to the extracellular matrix of bone cells. The presence of ZIF-8 nanoparticles was clearly detected on the pore wall of ZIF-8@Gel.

All hydrogels exhibited pore sizes distributed within 40–70 μm, with most concentrated in the range of 50–60 μm (Fig. S4). The diameter of osteoblasts is approximately 10–30 μm, and ideal scaffold pore sizes should facilitate cell infiltration and migration [66]. Therefore, the hydrogel scaffolds prepared in this study ensured that osteoblasts could penetrate the pores to form multipoint adhesion, promoting actin cytoskeleton reorganization and activation of proliferation/differentiation signals. Additionally, the porosity of three independent hydrogel replicates was determined via the ethanol displacement method. As shown in Fig. S5, the average porosities of Gel, ZIF-8@Gel, Exo@Gel, and Z/E@Gel were 79.0 %, 78.4 %, 78.1 %, and 77.2 %, respectively. ZIF-8 and MSC-Exos were primarily loaded on the pore walls of GelMA hydrogels, thus exerting no significant impact on their pore size and porosity. Typically, implants with high porosity (>70 %) can accelerate the excretion of metabolic products such as lactate, maintain microenvironmental pH stability, and reduce acidic inhibition of osteogenic differentiation [67]. Therefore, the hydrogel scaffolds prepared herein possess appropriate pore sizes and porosities to support cell migration and nutrient diffusion. Moreover, the immunofluorescence imaging technique was utilized to visualize the three-dimensional spatial distribution of MSC-Exos within the hydrogel. Imaging of PKH67-labeled MSC-Exos reveals a uniform distribution of MSC-Exos throughout the hydrogel, with the cylindrical profile clearly observable. The three-dimensional imaging of the white-boxed area can also verify the homogeneous distribution of MSC-Exos within the bulk hydrogels.

Exosomes enter cells through plasma membrane fusion or endocytosis, releasing their contents and exerting biological effects [68]. MSC-Exos encapsulated in Z/E@Gel were labeled with PKH67 to assess the uptake of released exosomes in osteogenesis-related cells. As depicted in Fig. 4(C), following 12-h co-incubation with Z/E@Gel, remarkable green fluorescence was detected in BMSCs, HUVECs, and

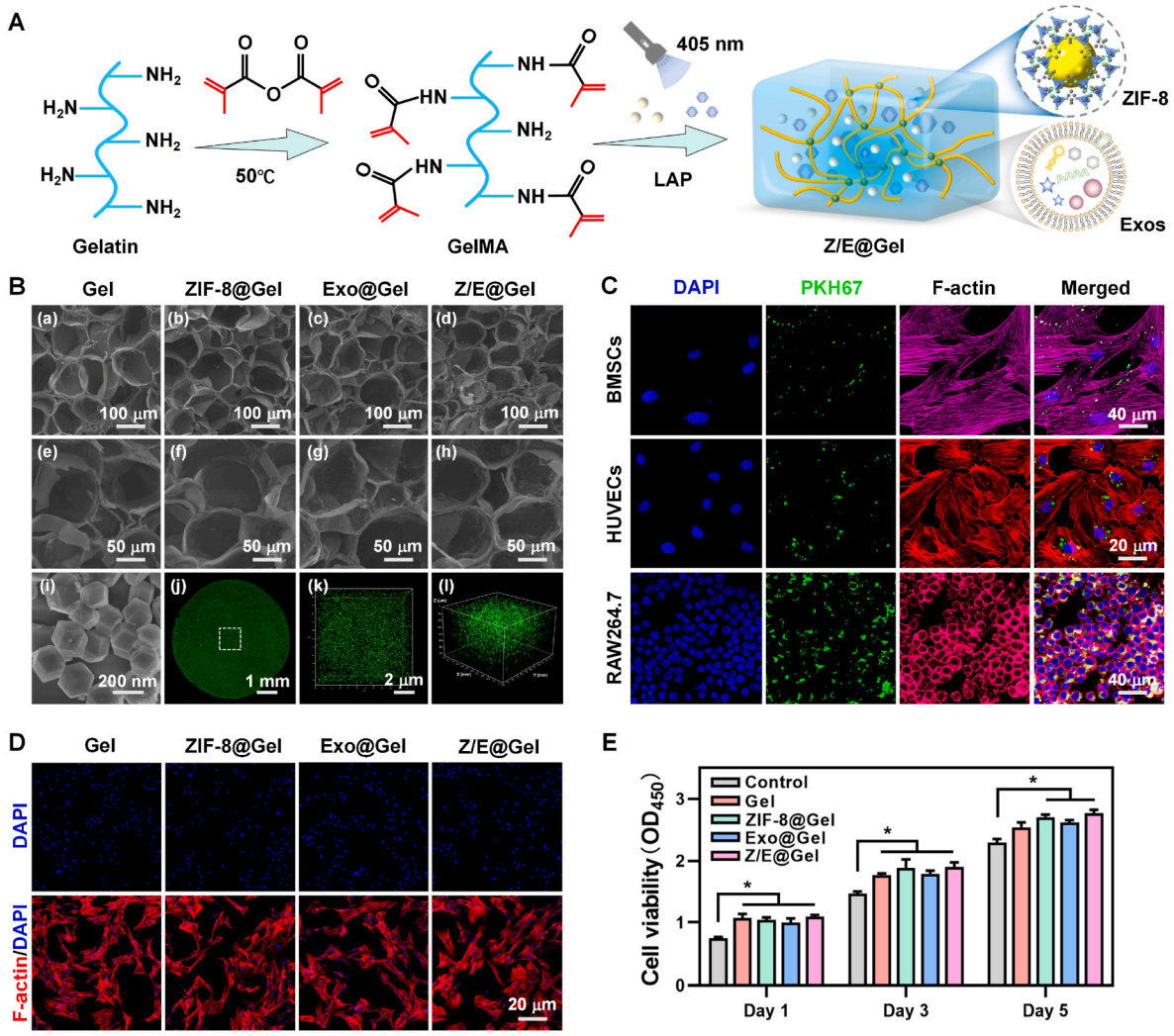

Fig. 4. Biocompatibility evaluation of the composite hydrogels. (A) Schematic illustration of the composite hydrogel encapsulating ZIF-8 and MSC-Exos. (B) Cross-sectional SEM images of the hydrogels (a–h), SEM image of ZIF-8 nanoparticles on the pore walls of ZIF-8@Gel (i), three-dimensional images of PKH67-labeled MSC-Exos in Z/E@Gel (j–l). (C) Uptake of PKH67-labeled MSC-Exos by BMSCs, HUVECs, and RAW264.7 cells. (D) Morphological observation of BMSCs on the surface of hydrogels. (E) CCK-8 assay of BMSCs incubated with the hydrogels. All data are presented as the mean ± SD (n = 3), *p < 0.05, compared with the control group.

RAW264.7 cells. The effective endocytosis of MSC-Exos in the cells suggests that MSC-Exos can facilitate bone tissue regeneration through multiple pathways, such as promoting osteogenic differentiation, inducing angiogenesis, and regulating inflammatory responses. Notably, the internalization efficiency of MSC-Exos exhibited marked heterogeneity across different cell types, with a significantly elevated intracellular distribution observed in RAW264.7 macrophages. Macrophages serve as core cells of the innate immune system, with high surface expression of scavenger receptors (CD36, SR-A), integrins (CD11b, CD18), and Toll-like receptors (TLRs). These receptors directly recognize signals such as phosphatidylserine and heat shock proteins on the surface of exosomes [69,70]. MSC-Exos carry tetraspanins (CD9, CD63), integrins, and immunomodulatory proteins (HSP70) on their surface, exhibiting high affinity for receptors like TLR4 and CD14 on macrophages, thus promoting active targeted uptake [71,72]. Meanwhile, emerging evidence indicates that the phagocytic activity of RAW264.7 cells is significantly enhanced following inflammatory stimulation, thereby facilitating efficient uptake of exosomes through multiple mechanisms, including macropinocytosis and receptor-mediated endocytosis [73]. In contrast, BMSCs primarily uptake exosomes via clathrin-dependent endocytosis or caveolin-mediated pinocytosis, with lower efficiency and reliance on specific ligand-receptor pairing mechanisms [74]. As endothelial barrier cells, HUVECs mainly uptake exosomes through transmembrane transport, mediated by adhesion molecules like ICAM-1 or selectins, with efficiency limited by cell junction tightness [75].

Cell morphology serves as an indicator of cellular physiological state and function. The nuclei (blue) and actin cytoskeleton (red) of BMSCs incubated with hydrogels are presented in Fig. 4(D). BMSCs in each group exhibited a polygonal morphology with extended filopodia that interconnected with adjacent cells. Meanwhile, the protrusions of elongated cells contribute to intercellular interactions and signal transduction. There was no statistically significant difference in the adhesion density of BMSCs in each group, suggesting that the MSC-Exos and ZIF-8-encapsulated hydrogels possess excellent biocompatibility (Fig. S6). The proliferation of BMSCs cultured with hydrogels was quantitatively assessed using the CKK-8 assay (Fig. 4(E)). In comparison with the control group, cell activity in all hydrogel groups was significantly enhanced on both the first and third days, indicating the superior biocompatibility of the GelMA hydrogel. On the fifth day, the ZIF-8@Gel, Exo@Gel, and Z/E@Gel groups still presented enhanced cell viability. These findings collectively demonstrate that ZIF-8 and MSC-Exos could significantly improve the biological activity of GelMA hydrogels, providing new opportunities for tissue engineering and regenerative medicine.

3.4. Osteogenic differentiation in vitro

During bone formation, BMSCs differentiate into osteoblasts, which subsequently synthesize the bone matrix. This matrix then undergoes mineralization to form mature bone tissue. The osteogenic capacity of BMSCs could be effectively assessed through the detection of osteogenesis-related markers. ALP expression initiates in the early stages of osteogenic differentiation and progressively increases as osteoblasts mature [76]. In the advanced stages of osteogenic differentiation, the ECM progressively undergoes mineralization, forming hard bone tissue [77]. As shown in Fig. 5(A), ALP and ARS staining were conducted on BMSCs cultured with the hydrogels following osteogenic induction. ALP expression levels and ECM mineralization levels in the ZIF-8@Gel, Exo@Gel, and Z/E@Gel groups were markedly elevated compared to the control and Gel groups (Fig. S7A and B). Meanwhile, the Z/E@Gel group manifested the highest expression levels of osteogenic markers, suggesting that mesenchymal stem cell exosomes and ZIF-8 can collaboratively facilitate osteogenesis. The ALP activity assay further indicates that Z/E@Gel elicits the highest level of ALP expression (Fig. 5(B)).

Furthermore, the expressions of OCN and Col I in BMSCs following 14 days of osteogenic induction were assessed via immunofluorescence and illustrated in Fig. 5(C and D). OCN is one of the most abundant non-collagen proteins in the bone matrix, and it is secreted by mature osteoblasts [78]. The expression of OCN is commonly recognized as a marker for osteoblast differentiation and maturation. Type I collagen, the predominant collagen in bone, constitutes over 90 % of the organic matrix [79]. OCN and Col I constitute the organic matrix within osteoblasts and serve fundamental roles in the bone mineralization process. The quantitative statistical results indicate that the Z/E@Gel group possesses the highest expression levels of OCN and Col I, similarly revealing the synergistic effect of MSC-Exos and ZIF-8 in promoting osteogenic differentiation of BMSCs (Fig. S7C and D). The expression of osteogenesis-related genes in Fig. 5(E) also provided evidence of the excellent osteoinductive properties of the Z/E@Gel hydrogel, which demonstrated superiority to the single-component hydrogel. MSC-Exos can deliver bioactive molecules to BMSCs, thereby enhancing their osteogenic differentiation. Concurrently, the zinc ions released from ZIF-8 function as the active centers of numerous enzymes and are

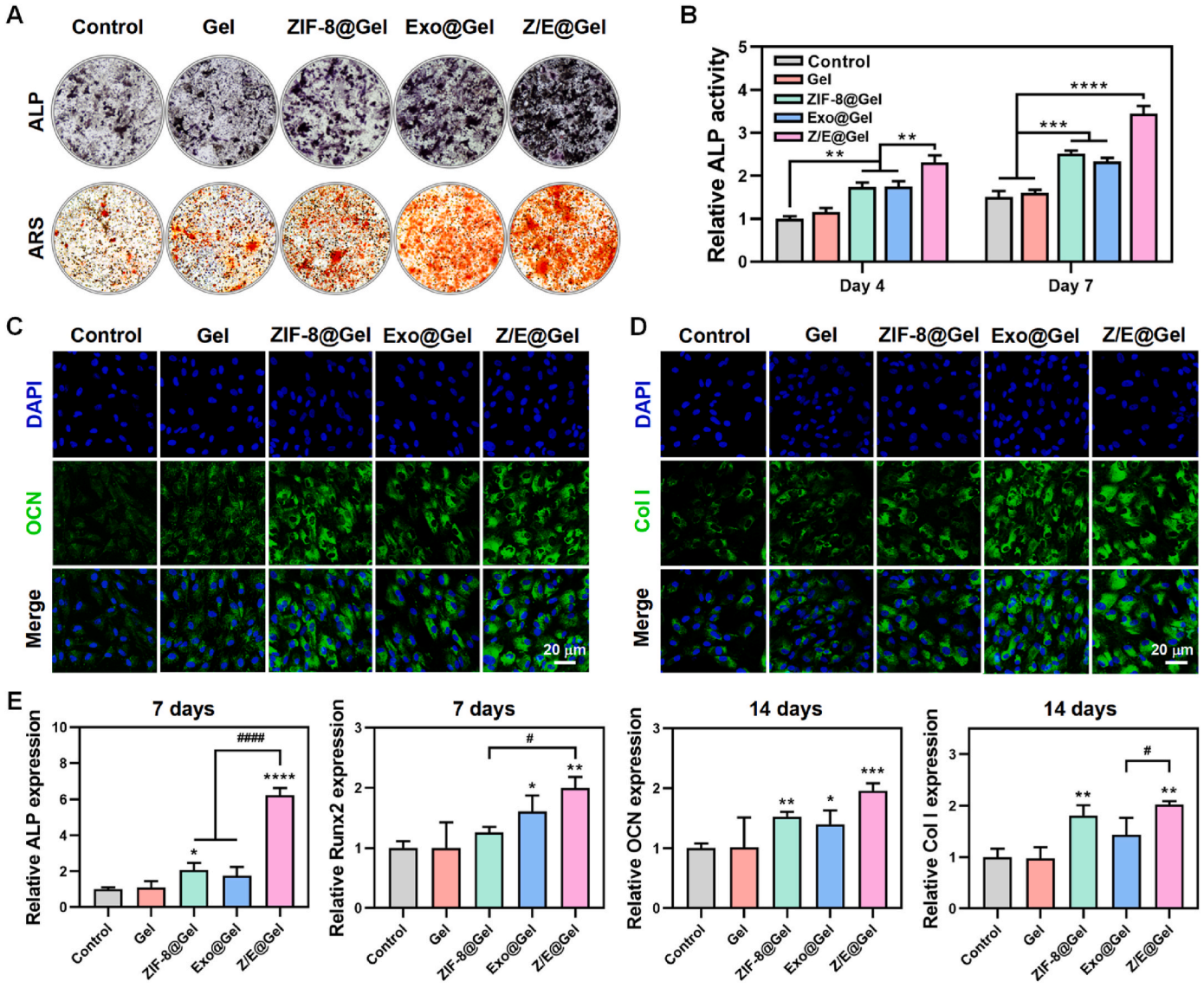

Fig. 5. Osteogenic differentiation of BMSCs incubated with the hydrogels *in vitro*. (A) ALP and ARS staining of BMSCs after osteogenic induction. (B) ALP activity of BMSCs after osteogenic induction. (C) Immunofluorescence staining of OCN in BMSCs. (D) Immunofluorescence staining of Col I in BMSCs. (E) Expression of osteogenesis-related genes. All data are presented as the mean ± SD (n = 3), * or #p < 0.05, ** or ##p < 0.01, *** or ###p < 0.001, **** or ####p < 0.0001, compared with the control group.

implicated in processes such as cell signal transduction and gene expression regulation, thereby exerting a facilitative effect on osteogenic differentiation. These results indicate that ZIF-8 and MSC-Exos can collaboratively regulate the expression of osteogenic genes and proteins, thereby promoting the osteogenic differentiation of BMSCs.

Bone remodeling represents a dynamic process characterized by the persistent regeneration of bone tissue, which relies on the establishment of new blood vessels to facilitate metabolic functions [80,81]. The newly formed blood vessels can transport blood to the defect area and supply the necessary oxygen and nutrients to repair bone tissue. A well-developed vascular network also improves local immune responses and minimizes the risk of delayed bone healing caused by infection [82]. The innermost layer of blood vessels is constituted by endothelial cells, which are crucial for angiogenesis. Endothelial cells exhibit the capacity to proliferate, migrate, and assemble into tubular structures, ultimately facilitating vascularization. For the purpose of evaluating the impact of hydrogels on angiogenesis, the migration and tube formation of HUVECs pretreated with hydrogel extracts were investigated (Fig. S8). The scratch assay results shown in Fig. S8(A, C) indicate that the migration rate of HUVECs was significantly increased in the ZIF-8@Gel, Exo@Gel, and Z/E@Gel groups, with the Z/E@Gel group demonstrating the highest migration rate. Few capillary tube structures were detected in both the control and Gel groups, indicating a limited angiogenic potential of HUVECs (Fig. S8B). Conversely, more mature and intact tubular structures, along with higher cell connection densities, could be observed in the ZIF-8@Gel, Exo@Gel, and Z/E@Gel groups. The quantitative statistics of tube length demonstrate that both Exo@Gel and Z/E@Gel possess a high tube formation capacity (Fig. S8D). It has been reported that exosomes can facilitate the angiogenesis of HUVECs by modulating the expression levels of cyclin D1 and D3 in HUVECs through the delivery of their internal miRNAs [83]. Concurrently, zinc ions are capable of regulating the expression of VEGF in HUVECs by influencing the activity of transcription factors such as zinc finger proteins [84]. The aforementioned analysis indicates that the significant angiogenic potential of Z/E@Gel primarily stems from the coordinated release of MSC-Exos and zinc ions, which effectively promote the angiogenesis of HUVECs.

3.5. Analysis of the osteogenesis mechanism

The osteogenic effect of MSC-Exos is affected by various components, such as proteins, lipids, mRNA, miRNA, and lncRNA. Furthermore, the genetic information in MSC-Exos may also change in accordance with the source, culture conditions, and physiological status of MSCs. The molecular mechanism through which MSC-Exos modulates osteogenesis is intricate and involves the interaction of multiple nucleic acid components. In the scope of this study, greater emphasis is placed on the influence of alterations in exosomal miRNAs on the osteogenic ability of MSC-Exos. Currently, miRNAs are the most studied nucleic acid components in exosomes [85,86]. They can regulate osteogenic

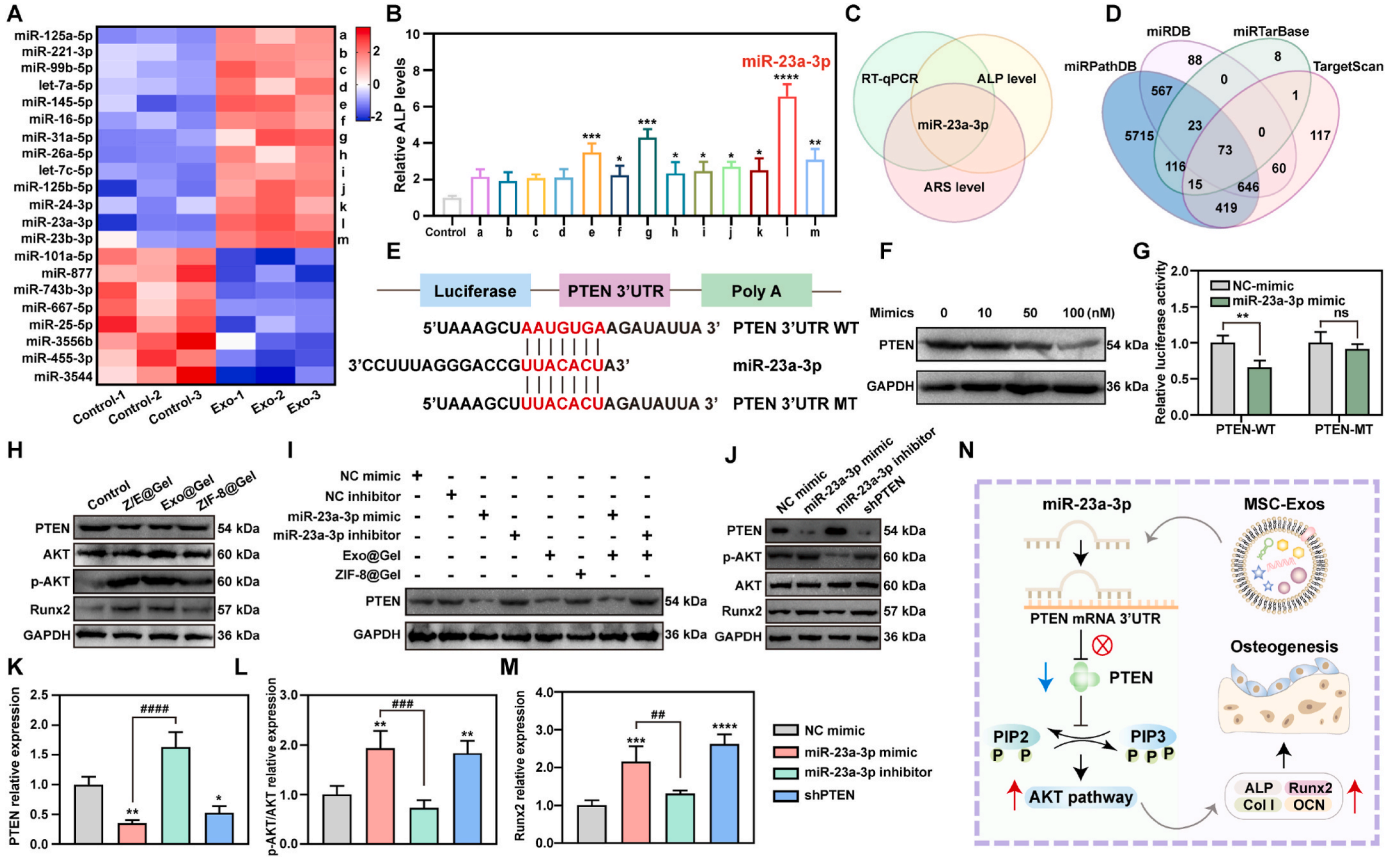

Fig. 6. Molecular mechanism of MSC-Exos induced osteogenic differentiation of BMSCs. (A) Heatmaps of the differentially expressed miRNAs of MSC-Exos (The control group represents MSC-Exos isolated from the third-generation BMSCs without osteogenic induction). (B) ALP activity assay of BMSCs transfected with miRNA mimics up-regulated in the osteogenic MSC-Exos. (C) Venn diagram analysis of miRNAs that significantly promote the osteogenic differentiation of BMSCs. (D) Potential mRNA targets of miR-23a-3p identified by four independent online databases. (E) Binding sites of miR-23a-3p in the PTEN 3′-UTR region. (F) Expression of PTEN protein after transfection of different concentrations of miR-23a-3p mimic in BMSCs. (G) Dual luciferase report between miR-23a-3p and PTEN. (H) Protein expression of PTEN, AKT, p-AKT, and Runx2 in BMSCs incubated with different hydrogels. (I) Regulation of PTEN protein expression in BMSCs by miR-23a-3p. (J) Regulation of the AKT pathway in BMSCs by miR-23a-3p and PTEN. (K) Relative expression of PTEN protein. (L) Quantitative statistics of the ratio of phospho-AKT (p-AKT) relative to AKT. (M) Relative expression of Runx2 protein. (N) Schematic illustration of the mechanism of miR-23a-3p regulating osteogenesis of BMSCs. All data are presented as the mean ± SD (n = 3), * or #p < 0.05, ** or ##p < 0.01, *** or ###p < 0.001, **** or ####p < 0.0001, compared with the control group.

differentiation by targeting mRNAs to inhibit the expression of specific genes. According to J. Xu et al., nine exosomal miRNAs showed significant upregulation following a 7-day osteogenic induction in BMSCs, while four miRNAs exhibited downregulation [87]. A. Liu et al. demonstrated that the osteogenic induction of BMSC-OI-exo is attributable to multiple exosomal miRNAs through a combination of bioinformatics analysis of miRNA microarrays and *in vitro* pathway validation of gene silencing and miRNA transfection [49]. These findings demonstrate that exosomal miRNAs exhibit significant alterations during the osteogenic differentiation process in BMSCs, which in turn impacts the osteogenic induction capacity of MSC-Exos.

In accordance with the miRNA sequencing results presented by A. Liu et al., a selection of miRNAs exhibiting notable differential expression in MSC-Exos prior to and following bone induction treatment was identified and validated through qPCR. As illustrated in Fig. 6(A), the expression of 14 miRNAs was up-regulated, while the expression of 8 miRNAs was down-regulated in MSC-Exos following osteogenic induction. MSC-Exos delivers exogenous miRNAs to BMSCs, targeting the degradation of osteogenesis-related mRNAs or suppressing their translation, thereby negatively modulating gene expression and subsequently influencing osteogenic differentiation. Consequently, the highly expressed 14 miRNAs in osteogenic MSC-Exos are the key sources of their bone-induction properties. The mimics of the highly expressed miRNAs in osteogenic MSC-Exos were transfected into BMSCs, and the resulting osteogenic activity was evaluated (Fig. S9). The mineralization level of ECM was significantly enhanced after BMSCs were transfected with miR-23a-3p mimic. Fig. 6(B) demonstrates that following transfection with the mimics of miR-145–5p, miR-31a-5p, miR-23a-3p, and miR-23b-3p, the osteogenic differentiation of BMSCs was improved, with the miR-23a-3p mimic exhibiting the most pronounced osteogenic-promoting performance. The combined analysis of RT-qPCR of miRNAs, ALP activity, and ECM mineralization demonstrates that miR-23a-3p in MSC-Exos contributes substantially to regulating bone-inducing performance (Fig. 6(C)).

The identification of the target genes of miR-23a-3p is of paramount importance for the elucidation of the osteogenic mechanism of MSC-Exos. Underlying mRNA targets of miR-23a-3p were predicted based on four independent online databases: miRPathDB, miRDB, miRTarBase, and TargetScan. As illustrated in Fig. 6(D), a total of 73 potential mRNA targets were identified across all four databases. To further precisely define the scope of mRNA targets, the mRNAs related to osteogenic differentiation were screened from the 73 mRNAs through the g: GOSt tool of the G: Profiler online website. DDX5, FBN2, FGF2, and PTEN were recognized to be involved in osteoblast differentiation (Fig. S10). PTEN (phosphatase and tensin homolog) has been extensively reported as an important node in osteogenic differentiation [88,89]. After the knockout of PTEN in osteoblasts, the protein kinase B (AKT) signaling pathway is activated, thereby inducing osteoblast proliferation and increasing bone mass [90]. Fig. 6(E) presents the recognition sites of miR-23a-3p with the wild-type and mutant 3′UTR of PTEN. In order to evaluate the impact of miR-23a-3p on the PTEN protein expression level, BMSCs were transfected with miR-23a-3p mimics at varying concentrations (Fig. 6(F)). With the increase in the concentration of the transfected miR-23a-3p mimics, the expression level of the PTEN protein in BMSCs gradually decreased, indicating the inhibitory effect of miR-23a-3p on its potential target gene PTEN (Fig. S11A). Subsequently, a dual luciferase reporter gene vector containing the 3′UTR sequence of PTEN was constructed and co-transfected with miR-23a-3p mimics or NC mimics into BMSCs to detect luciferase activity. The quantitative statistics in Fig. 6(G) demonstrate that after transfection with miR-23a-3p mimics, the luciferase activity of wild-type PTEN significantly decreased compared with that after transfection with NC mimics, while no significant change was observed in the expression of mutant PTEN, thereby verifying PTEN as the target of miR-23a-3p.

Based on the confirmation that PTEN is a direct target of miR-23a-3p, it is reasonable to hypothesize that PTEN may serve as a critical regulator in exosomal miRNA-mediated osteogenic differentiation of BMSCs. To validate this hypothesis, BMSCs were co-transfected with PTEN-overexpressing plasmids and miR-23a-3p mimics, followed by assessment of the expression levels of osteogenesis-related proteins. As shown in Fig. S12, transfection of miR-23a-3p mimics into osteogenically induced BMSCs significantly enhanced the expression of osteogenesis-related proteins. Concurrently, miR-23a-3p downregulated PTEN expression in BMSCs. However, overexpression of PTEN attenuated the osteogenic promotion mediated by miR-23a-3p. Specifically, the expression levels of OCN and Col I proteins in the PTEN + miR-23a-3p mimic group were significantly lower than those in the miR-23a-3p mimic group. Therefore, it can be concluded that PTEN plays a key role in miR-23a-3p-mediated osteogenic differentiation, and overexpression of PTEN significantly inhibits the osteogenic differentiation of BMSCs.

It is widely recognized that the AKT signaling pathway is crucial for regulating the osteogenic differentiation of BMSCs [91–93]. AKT affects cell cycle, survival, and metabolism by phosphorylating downstream target proteins, including mTOR, FOXO, GSK3β, etc., thereby facilitating osteogenic differentiation [94]. The association between PTEN and AKT is evidenced by the suppressive effect of PTEN on the AKT signaling pathway [95]. PTEN reduces PIP3 levels by removing the 3-phosphoryl group from PIP3 via its phosphatase activity, thereby generating phosphatidylinositol-4,5-bisphosphate (PIP2) [96]. Given that PIP3 is a prerequisite for AKT activation, the inhibitory effect of PTEN precludes the effective recruitment of AKT to the cell membrane, thereby suppressing the activation of the AKT pathway and the osteogenic differentiation of BMSCs [97]. Conversely, PTEN deficiency leads to significantly elevated AKT phosphorylation [98]. Therefore, silencing or downregulating PTEN (e.g., via miRNA targeting or protein interaction inhibition) relieves its inhibitory effect on the AKT pathway, promoting osteogenic differentiation of BMSCs [99].

Based on the aforementioned analysis, it is plausible to conclude that miR-23a-3p activates the AKT signaling pathway by targeting and suppressing PTEN expression. The protein expression levels of PTEN, AKT, p-AKT, and Runx2 in BMSCs incubated with the hydrogels were analyzed by Western blot and illustrated in Fig. 6(H). Compared to the control and ZIF-8@Gel groups, the expression levels of PTEN protein decreased in the Z/E@Gel and Exo@Gel groups, while the expression levels of p-AKT and Runx2 were significantly increased (Fig. S11B). There were no significant differences in AKT expression across the groups, while Runx2 expression was positively correlated with p-AKT (Fig. S11C–E). Consequently, MSC-Exos is capable of facilitating the phosphorylation of AKT by reducing the expression of PTEN, thereby upregulating the expression of osteogenic proteins.

To elucidate the regulatory role of miR-23a-3p on the target gene PTEN, the impact of miR-23a-3p mimics and inhibitors on the expression of PTEN protein in BMSCs was further examined (Fig. 6(I)). As presented in Fig. S13, both miR-23a-3p mimic and Exo@Gel significantly down-regulated the expression of PTEN protein, while miR-23a-3p inhibitor up-regulated the expression of PTEN protein. The combined effect of the miR-23a-3p mimic and Exo@Gel resulted in a further reduction in PTEN protein expression. Conversely, the miR-23a-3p inhibitor was able to reverse this reduction in PTEN expression. These findings further validate that miR-23a-3p in MSC-Exos can target and regulate the expression of PTEN in BMSCs. Meanwhile, to clarify the impact of miR-23a-3p and PTEN on the activation of the AKT pathway, miR-23a-3p mimic, miR-23a-3p inhibitor, and the vector carrying the PTEN gene-specific short hairpin RNA (shPTEN) were transfected into BMSCs, and the expressions of p-AKT and the downstream osteogenic factor Runx2 were evaluated (Fig. 6(J-M)). The PTEN expression was remarkably decreased in the miR-23a-3p mimic and shPTEN groups, while the p-AKT and Runx2 expression were increased. In contrast, the expression of PTEN was increased in the miR-23a-3p inhibitor group, while the expressions of p-AKT and Runx2 were decreased. Therefore, it

can be concluded that miR-23a-3p in MSC-Exos activates the AKT signaling pathway by inhibiting the expression of the target gene PTEN, thereby promoting the downstream osteogenic gene expression (Fig. 6 (N)).

3.6. Immunomodulatory property assessment in vitro

Bone repair is a complex, multistage process involving three key phases: the inflammatory response, new bone formation, and remodeling [100]. As a crucial immune system constituent, macrophages are a critical factor in tissue repair and inflammatory reactions [101,102]. In the initial stage of bone repair, M1 macrophages contribute to eliminating necrotic bone and infection, creating favorable conditions for new bone formation. However, an excessive M1 macrophage response might also result in tissue damage and delayed repair [103]. During the later phase of the inflammatory response, the gradually increasing number of M2 macrophages initiates the repair of damaged bone tissue by secreting factors that facilitate bone formation and angiogenesis [104]. Therefore, the development of hydrogels with active guidance of macrophage polarization towards a regenerative M2 phenotype could enable immune-mediated bone regeneration. In this study, RAW264.7 cells were employed as the model macrophages and stimulated with LPS to simulate the initial inflammatory response after implantation.

As depicted in Fig. 7(A), CCR7 and CD206 were utilized to label M1 and M2 macrophages, and the transformation of macrophage polarization phenotypes was quantitatively assessed based on flow cytometry. Based on a well-defined flow cytometry gating strategy in Fig. S14, quadrants Q1, Q2, Q3, and Q4 were designated to represent M1 macrophages, double-positive cells, unpolarized macrophages, and M2 macrophages, respectively. LPS significantly induced RAW264.7 cells to polarize into M1 macrophages in both the control and Gel groups. The proportions of CCR7-positive macrophages were 55.8 % and 58.2 %, respectively, and there were scarcely any CD206-positive macrophages. The high proportion of M1 polarization in the control and Gel groups suggests that macrophages are hard to spontaneously transform from the pro-inflammatory M1 type to the anti-inflammatory M2 type in the absence of external intervention or cytokines. On the other hand, the expression of CD206 was found to be considerably higher in the ZIF-

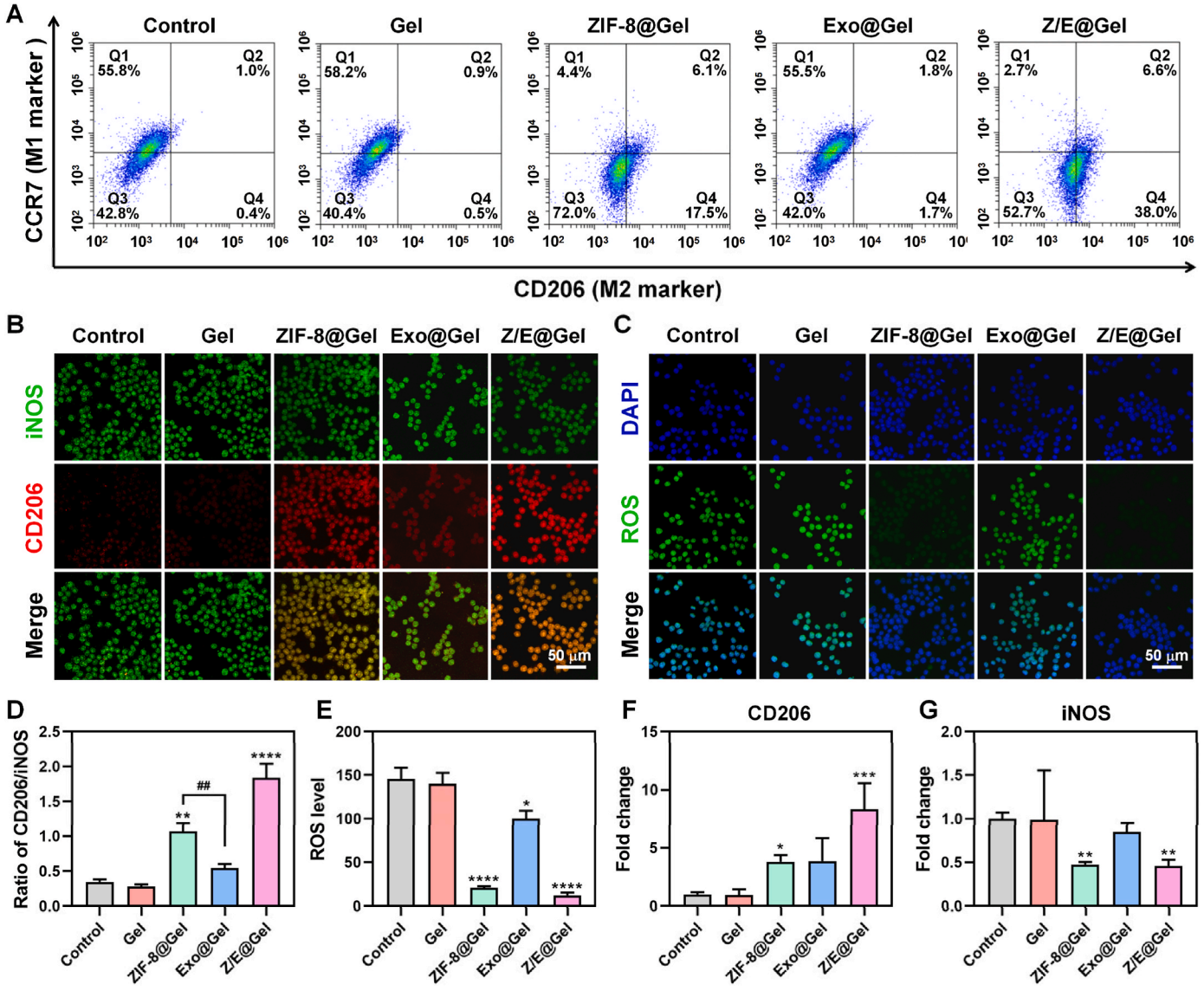

Fig. 7. Evaluation of the immunomodulatory properties of the hydrogels. (A) Polarization of RAW264.7 cells analyzed by flow cytometry. (B) Immunofluorescence staining of iNOS and CD206. (C) Fluorescent images of intracellular ROS. (D) The intensity ratio of CD206 and iNOS in immunofluorescence images. (E) Quantitative statistics of intracellular ROS levels. (F) Quantification of CD206 expression by qPCR. (G) Quantification of iNOS expression by qPCR. All data are presented as the mean ± SD (n = 3), * or #p < 0.05, ** or ##p < 0.01, *** or ###p < 0.001, **** or ####p < 0.0001, compared with the control group.

8@Gel and Z/E@Gel groups, in contrast to a notable reduction in CCR7 expression. This finding confirms that the outstanding immunomodulatory performance of ZIF-8 is conducive to the transition of macrophages from M1 to M2 phenotype, thereby creating an immune microenvironment suitable for osteogenesis. Meanwhile, the polarization phenotype of RAW264.7 cells in the Exo@Gel group exhibited no significant change compared to the control group, corresponding to the weak immunomodulatory property of MSC-Exos. During the osteogenic differentiation process, the cellular phenotype and function of BMSCs undergo transformation, leading to changes in their initial immunomodulatory characteristics. Previous studies have also identified the deteriorated immunomodulatory performance of bone-functionalized exosomes secreted by osteogenic pre-differentiated BMSCs [30].

CD206 is typically expressed at elevated levels in M2 macrophages and plays a critical role in various processes, including anti-inflammatory responses, tissue repair, and the clearance of cell debris [105]. The expression of iNOS in M1 macrophages is markedly enhanced, thereby augmenting inflammatory responses and potentiating cytotoxic effects [106]. Immunofluorescence staining in Fig. 7(B) further confirmed that the expression of CD206 was remarkably enhanced in the ZIF-8@Gel and Z/E@Gel groups, while the expression of iNOS was reduced. The quantitative analysis of fluorescence intensity indicates that the CD206 to iNOS ratio in the ZIF-8@Gel and Z/E@Gel groups is markedly elevated compared to the other experimental groups (Fig. 7(D)). Consistent with the flow cytometry results, the M2 polarization level in the Z/E@Gel group was significantly higher than that in the ZIF-8@Gel group. The data point to the possibility that ZIF-8 can rejuvenate the immunomodulatory characteristics of MSC-Exos. As illustrated in Fig. S15, CD86 immunofluorescence staining (M1 macrophage marker) in LPS-induced RAW264.7 cells further bolsters the credibility of the findings. Quantitative analysis in Fig. S16 revealed that the ZIF-8@Gel and Z/E@Gel groups exhibited statistically significant downregulation of CD86 expression compared to both the control and Gel groups, whereas no statistically significant differences were observed between the Gel group and control group. These collective data confirm the outstanding anti-inflammatory properties of ZIF-8 in hydrogels.

Additionally, it was observed that LPS-induced RAW264.7 cells produced elevated levels of ROS, as illustrated in Fig. 7(C). Elevated levels of ROS have been shown to impair the bone microenvironment, thereby exacerbating oxidative stress and inflammatory responses, which consequently exert a deleterious effect on the osteogenic process [107]. The quantitative statistics in Fig. 7(E) indicate that the ROS levels of RAW264.7 cells in the ZIF-8@Gel and Z/E@Gel groups have decreased significantly, corresponding to their higher proportion of M2 polarization. As presented in Fig. 7(F, G) and Fig. S17, the qPCR results of immune regulation-related genes demonstrated that the expressions of M2 phenotype markers, including CD206, Arg-1, and IL-10, were markedly enhanced in the ZIF-8@Gel and Z/E@Gel groups. Conversely, the expressions of M1 phenotype markers, such as iNOS, TNF-α, and IL-6, exhibited relatively low levels. These findings jointly demonstrate that the Z/E@Gel effectively reduces inflammatory responses and promotes bone tissue regeneration by inducing a transition of macrophages from M1 to M2 phenotype in an inflammatory setting.

3.7. Investigation of immunomodulatory mechanism

As previously stated, the ZIF-8 loaded in the composite hydrogels demonstrated outstanding immunoregulatory performance, effectively compensating for the insufficiency of the immunoregulatory performance of bone-functionalized MSC-Exos. The immunomodulatory mechanism of ZIF-8 has attracted increasing attention. Wang et al. suggest that the immunomodulatory mechanism of ZIF-8 may involve ions released during its biodegradation as well as its induced biomineralization processes [39]. These processes jointly act on the local microenvironment to regulate the immune response and facilitate osteogenesis. Unfortunately, current work does not reveal the molecular mechanism of ZIF-8 in immunomodulation, greatly limiting the application of ZIF-8 as a safe and readily available immunomodulator. This work employs RNA sequencing, bioinformatics analysis, and molecular biological approaches to investigate the molecular mechanisms of ZIF-8 in immunomodulation.

As depicted in Fig. 8(A), KEGG pathway enrichment analysis was conducted for the DEGs in the control and ZIF-8@Gel groups, and the top 16 significantly enriched pathways were presented. NF-κB and TNF signaling pathways that are closely associated with immune regulation were enriched. Meanwhile, it was observed that ZIF-8 had a remarkable influence on the osteoclast differentiation of RAW264.7 cells. Among them, the NF-κB pathway is a crucial signal transduction route in immune regulation, exerting a significant role in modulating inflammatory responses, cell proliferation, differentiation, and apoptosis [108,109]. The NF-κB pathway is typically initiated by multiple extracellular stimuli, such as bacterial LPS, CpG oligonucleotides, and tumor necrosis factor-alpha (TNF-α). LPS binds to the transmembrane protein Toll-like receptor 4 (TLR4) on the surface of macrophages, activating NF-κB family transcription factors in the cytoplasm [110]. In the resting state, NF-κB is sequestered in the cytoplasm by the inhibitory protein IκB. When macrophages are exposed to inflammatory stimuli, NF-κB is activated and translocates into the nucleus to regulate the transcription of target genes [111,112]. The volcano plot of the DEGs showed that 346 genes were up-regulated and 295 genes were down-regulated in the ZIF-8@Gel group compared to the control group (Fig. 8(B)). Among them, the transcription levels of genes related to the NF-κB signaling pathway, such as RelB and IL4, were significantly up-regulated in the ZIF-8@Gel group. The gene expression heatmap in the NF-κB signaling pathway further demonstrated significant differences in gene expression patterns between the control and ZIF-8@Gel groups (Fig. 8(C)). The GSEA analysis of DEGs also revealed that the NF-κB signaling pathway was positively enriched in the control group compared with the ZIF-8@Gel group (Fig. 8(D)). It can be hypothesized that ZIF-8 mitigates excessive inflammatory responses by inhibiting the activation of the NF-κB signaling pathway in LPS-induced RAW264.7 cells.

Protein-protein interaction network analysis was conducted on DEGs significantly enriched in the NF-κB pathway to identify the key nodes in the network, as shown in Fig. 8(E). It can be observed that P100 evidently occupies a core position in the PPI network and is closely linked to other proteins, suggesting the crucial role of this target in the NF-κB pathway. The NF-κB signaling pathway is typically classified into two pathways: the classical and the non-classical. P100 mainly participates in the non-classical NF-κB signaling pathway, also known as the NF-κB2 signaling pathway [113]. P100 combines with the P52 subunit in the cytoplasm to form a complex and binds to the inhibitory protein IκBα, maintaining the inactivity of the P100/P52 complex in the cytoplasm. The stability of P100 is regulated by the specific deubiquitinase OTUB1, which prevents P100 from being cleaved into P52 by inhibiting its ubiquitination and degradation, thereby suppressing the activation of the NF-κB signaling pathway [114]. When RAW264.7 cells were stimulated by LPS, the NF-κB signaling pathway was activated, leading to the degradation of IκBα and ubiquitination of P100. The P100 degraded by the proteasome releases the mature P52 subunit. Subsequently, P52 combines with the RelB subunit to form a dimer and enters the nucleus to activate the transcription of specific genes [115]. The distribution of P100/P52 in RAW264.7 cells was observed via immunofluorescence staining, as depicted in Fig. 8(F). Quantitative statistics reveal that a large portion of P100 in the cytoplasm of the control and Exo@Gel groups is degraded to P52 and enters the nucleus (Fig. 8(J)). By contrast, only a portion of the degraded P100 in the ZIF-8@Gel and Z/E@Gel groups entered the nucleus. This indicates that ZIF-8 can diminish the activation of the non-classical NF-κB signaling pathway induced by LPS, while the MSC-Exos has no notable influence. In contrast, only partially degraded P100 entered the nucleus in the ZIF-8@Gel and Z/E@Gel groups, indicating that ZIF-8 reduced LPS-induced activation of the

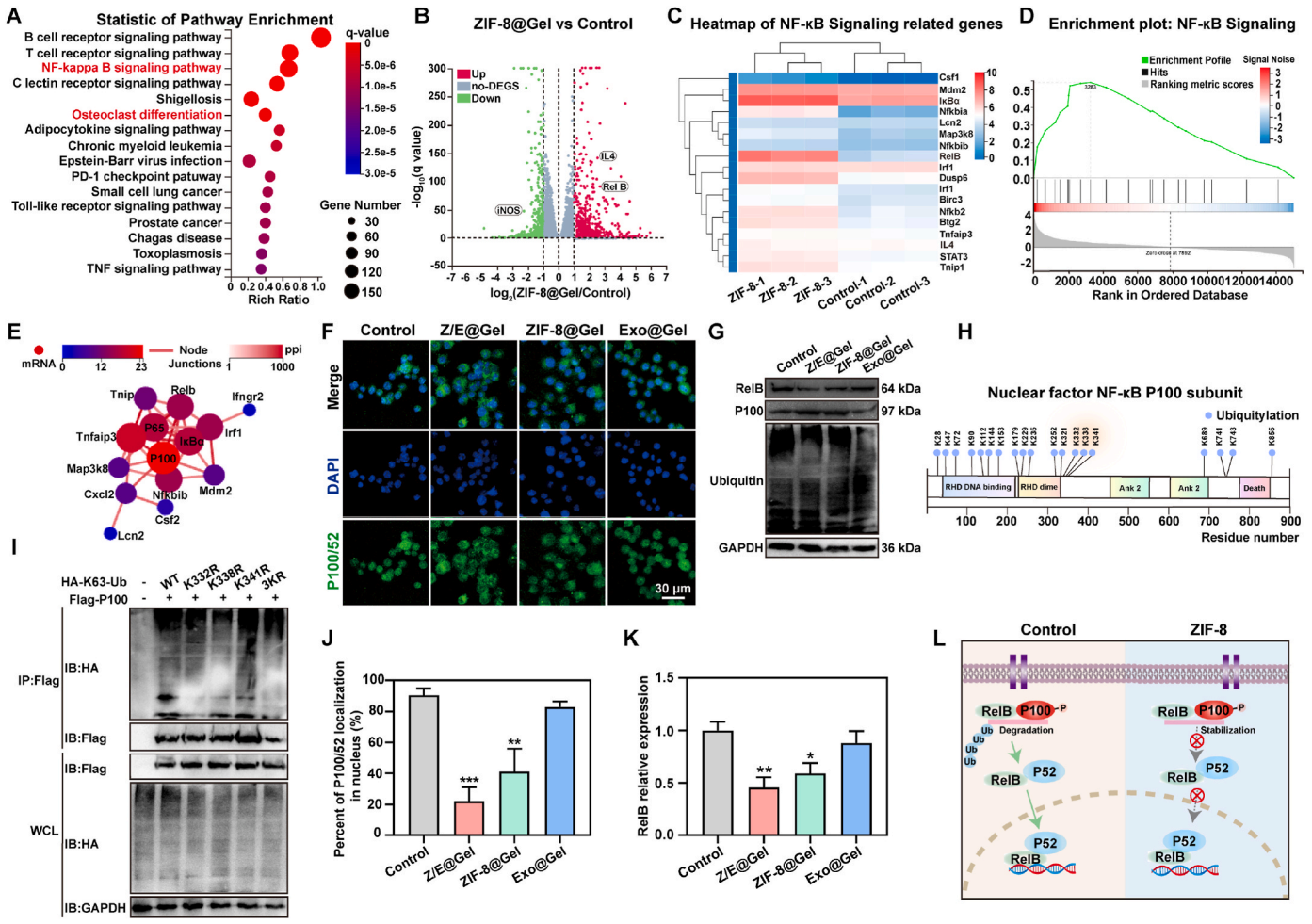

Fig. 8. Molecular mechanisms of ZIF-8 in immunomodulation. (A) KEGG pathway enrichment analysis of the differentially expressed genes (DEGs) between the control and ZIF-8@Gel groups. (B) Volcano plot of DEGs. (C) Heatmap of genes associated with the NF-κB signaling pathway. (D) Gene set enrichment analysis (GSEA) of gene sets associated with the NF-κB signaling pathway. (E) Protein-protein interaction network for the NF-κB signaling pathway. (F) Immunofluorescence images of P100/52 in RAW264.7 cells. (G) Expression of P100/52 and RelB in the nucleus and the overall ubiquitination level in RAW264.7 cells. (H) Identification of the ubiquitination sites of P100 protein. (I) Identification of potential ubiquitination sites of P100. (J) Percentage of P100/52 protein distributed in the nucleus. (K) The expression of P100 protein in RAW264.7 cells. (L) Schematic of the regulation of the non-classical NF-κB signaling pathway by ZIF-8. All data are presented as the mean ± SD (n = 3), *p < 0.05, **p < 0.01, ***p < 0.001.

non-classical NF-κB signaling pathway, whereas MSC-Exos had no significant effect.

P100 and RelB are stably associated in the cytoplasm in the inactive state. When the non-classical NF-κB signaling pathway is activated, the NF-κB inducing kinase (NIK) activates IKKα, and IKKα subsequently phosphorylates specific amino acid residues on the P100 protein [116]. Phosphorylated P100 undergoes ubiquitination, a process whereby a series of ubiquitin molecules (Ubiquitin) are added to the P100 protein [117]. The ubiquitination of P100 causes it to be recognized and cleaved by the proteasome, producing a P52/RelB heterodimer. The expression of RelB and P100, as well as the overall cellular ubiquitination level, was detected by Western blot (Fig. 8(G)). The expression of RelB in the nucleus of the ZIF-8@Gel and Z/E@Gel groups was markedly downregulated compared with that of the control group and the Exo@Gel group, while the total ubiquitination level of the RAW264.7 cell also exhibited a decreasing tendency (Fig. 8(K) and Fig. S18B). As discussed previously, the P52/RelB heterodimers are generated through the non-classical NF-κB signaling pathways, with the critical event being the proteolytic processing of P100 into P52. Inhibition of the non-classical NF-κB signaling pathway in the ZIF-8@Gel and Z/E@Gel groups leads to increased levels of undegraded P100 (Fig. S18A). It can be concluded that ZIF-8 reduces the activation of the non-classical NF-κB signaling pathway by suppressing the ubiquitination-mediated degradation of P100 and decreasing the entry of P52/RelB into the nucleus.

The foregoing analysis demonstrates that ZIF-8 is capable of suppressing the activation of the non-classical NF-κB signaling pathway by reducing the ubiquitination-mediated degradation of P100, thereby regulating the polarization phenotype of macrophages. Therefore, identifying potential ubiquitination sites of P100 is conducive to accurately understanding the immune regulatory mechanism of ZIF-8. Based on the prediction of potential ubiquitination sites of P100 from the PhosphoSitePlus online data (Version 6.7.5, NIH, USA) and the reports of Chen et al. [118], the potential ubiquitination sites of P100 include the lysine residues at positions K332, K338, and K341 (Fig. 8(H)). As shown in Fig. 8(I), the lysine at these sites was mutated to arginine, and the changes in the ubiquitination level of P100 were assessed. The ubiquitination level of P100 was reduced compared to the wild type when the lysine at positions K332 and K338 was mutated. The ubiquitination level of P100 was not significantly altered when the lysine at K341 was mutated in comparison to the wild type. When all three sites were mutated simultaneously, the ubiquitination level of P100 was diminished compared to the wild type. Therefore, the ubiquitination-mediated degradation of P100 is mediated by the two sites, K332 and K338. It can be concluded that ZIF-8 reduces the

cleavage of P100 to active P52 by reducing the ubiquitination at the sites K332 and K338 on P100 and ultimately reduces the activation of the non-classical NF-κB signaling pathway (Fig. 8(L)).

3.8. Biocompatibility evaluation of hydrogels in vivo

In view of the remarkable osteogenesis, angiogenesis, and immunomodulation exhibited by the GelMA hydrogel encapsulating MSC-Exos and ZIF-8 *in vitro*, a circular bone defect model was established on the skulls of SD rats to assess the bone-forming capacity *in vivo*. In bone defect repair, degradable hydrogel scaffolds are required to provide safe temporary mechanical support while creating space and guidance for new bone tissue, ultimately enabling permanent replacement by host tissues. Thus, the degradation behavior of artificially designed hydrogel materials must precisely match the bone healing/regeneration rate and avoid generating toxic degradation products. To evaluate the biodegradability and biosafety of composite hydrogels, remaining hydrogels were collected at 1, 2, and 4 weeks post-implantation, lyophilized, and weighed. As shown in Fig. S19, the degradation rates of ZIF-8@Gel and Z/E@Gel were slightly lower than that of Gel at the initial implantation stage, but no significant difference was observed among groups after 4 weeks. Z/E@Gel exhibited favorable biodegradability *in vivo*, with average mass retentions of 81.3 %, 62.5 %, and 33.6 % at 1, 2, and 4 weeks post-implantation, respectively. Given that the renewal cycle of normal bone tissue is approximately 4–8 weeks, the degradation of Z/E@Gel to 33.6 % within 4 weeks aligns with the timeline of bone self-repair, indicating that the material can serve as a temporary scaffold to guide bone regeneration.

At 1 and 4 weeks post-implantation, whole blood was collected via cardiac puncture from rats, and serum zinc ion concentrations were measured. As shown in Fig. S20, serum zinc ion concentrations in the Z/E@Gel and ZIF-8@Gel groups were comparable (18.81 μmol/L and 19.10 μmol/L at week 4, respectively) and not significantly different from the control group (19.33 μmol/L). The structure of ZIF-8 remains relatively stable under physiological conditions (neutral pH, 37 °C), with zinc ion release primarily dependent on slow degradation or ligand exchange processes rather than rapid dissolution. Additionally, encapsulation of ZIF-8 nanoparticles within the GelMA hydrogel network creates an effective physical barrier. Following release from ZIF-8, zinc ions must diffuse through the hydrogel network to enter the surrounding tissue fluid, significantly slowing their diffusion into systemic circulation. This combination of the intrinsic sustained release property of ZIF-8 and the diffusion barrier formed by GelMA constitutes an efficient dual-controlled release system, effectively preventing abrupt and excessive zinc ion influx into the bloodstream.

Furthermore, zinc ions released from the composite hydrogel initially accumulate in the tissue fluid and extracellular matrix at the implantation site. Key bone regeneration processes, including osteoblast activity, neovascularization, and matrix mineralization, actively sequester and utilize zinc ions [119,120]. Meanwhile, soft tissues and inflammatory/repair cells (e.g., macrophages, fibroblasts) surrounding the defect also uptake zinc ions for metabolic needs [121]. Additionally, a portion of released zinc ions binds to proteins such as albumin and transferrin in the local tissue fluid, forming macromolecular complexes [122]. This binding reduces the concentration gradient of free zinc ions and further retards their diffusion into blood vessels. In summary, the majority of zinc ions released from the hydrogel are localized to the implantation site and effectively utilized by newly formed bone tissues. Only a minimal fraction is gradually dispersed into the systemic circulation, with this additional zinc load remaining well within the robust homeostatic regulatory capacity of the organism, thereby insufficient to induce statistically significant alterations in serum zinc concentrations.

Following implantation of the hydrogel material into cranial defects, the expression levels of cytokines in local tissue fluids are closely associated with inflammatory responses and tissue repair processes. In the early surgical stage, tissue damage caused by bone defects activates immune cells such as macrophages and neutrophils, which rapidly release proinflammatory factors TNF-α and IL-6 to initiate the inflammatory response, recruiting immune cells to clear necrotic tissues and pathogens [123,124]. Consequently, high levels of TNF-α and IL-6 were observed in all groups 1 day post-implantation, as illustrated in Fig. S21. Due to the potential foreign body stimulation of the hydrogel material at the initial implantation stage, which transiently enhances proinflammatory factor release, the IL-6 level in the Z/E@Gel group was higher than that in the control group (bone defect without hydrogel implantation) 1 day post-implantation. The anti-inflammatory factor IL-10 was not significantly induced at this time, or was only preliminarily expressed by a small number of regulatory cells, resulting in extremely low levels in all groups. At 7 days post-implantation, TNF-α gradually decreased after reaching the inflammatory peak but remained at a certain level to regulate the migration and proliferation of fibroblasts and vascular endothelial cells [125]. In addition to being secreted by immune cells, IL-6 can also be produced by tissue cells such as fibroblasts and endothelial cells, whose expression is induced by upstream factors such as TNF-α and IL-1β, with a time lag in synthesis and release [126,127]. Therefore, the decline of IL-6 lagged behind that of TNF-α, remaining at a high level on day 7. Notably, the expression levels of TNF-α and IL-6 in the Z/E@Gel group were significantly lower than those in the control and Gel groups on day 7, while the expression level of IL-10 was significantly increased. At 28 days post-implantation, the levels of TNF-α, IL-6, and IL-10 in all groups significantly decreased. The Z/E@Gel group still maintained lower TNF-α and IL-6 levels, while IL-10 remained at a higher level, inhibiting secondary inflammation during the repair process and promoting extracellular matrix synthesis and vascular maturation to provide a microenvironment for bone matrix deposition [128,129]. In conclusion, Z/E@Gel can shorten the peak duration of proinflammatory factors and enhance the anti-inflammatory effect of IL-10 after *in vivo* implantation, thereby accelerating bone defect repair.

To evaluate hepatic and renal injury, serum levels of aspartate aminotransferase (AST), alanine aminotransferase (ALT), total bilirubin (TBIL), blood urea nitrogen (BUN), creatinine (CREA), and uric acid (UA) were systematically quantified in rats implanted with hydrogels using standardized biochemical assays. As shown in Fig. S22, all rats exhibited ALT, AST, and TBIL values within the normal range, excluding acute hepatocyte injury induced by the material. Meanwhile, BUN, CREA, and UA indicators also fell within healthy ranges, demonstrating normal glomerular filtration function and no purine metabolism disorders or renal excretory burden caused by hydrogel scaffold degradation. No statistically significant differences in hepatic/renal functional indices were observed between hydrogel-implanted groups and controls, with minor intergroup variations attributable to individual physiological differences rather than metabolic disturbances. Additionally, at 8 weeks post-hydrogel scaffold implantation, major organs (heart, liver, spleen, lung, and kidney) were subjected to H&E staining to assess *in vivo* biosafety. As shown in Fig. S23, H&E-stained sections of all major organs exhibited no significant histopathological abnormalities or structural changes, with normal tissue morphology, indicating that Z/E@Gel did not induce organ toxic reactions. Collectively, these results demonstrate that Z/E@Gel composite hydrogel did not trigger obvious systemic toxic reactions upon *in vivo* implantation, and its degradation products imposed no significant burden on liver and kidney functions.

3.9. Evaluation of bone formation in vivo

Eight weeks following the implantation surgery, the repair of the bone defects was evaluated via radiographic examination and histological analysis. As illustrated in Fig. 9(A), micro-CT imaging of the cranial defect region reveals a substantial enhancement in bone regeneration in the ZIF-8@Gel, Exo@Gel, and Z/E@Gel groups, as compared to the control and Gel groups. Notably, the bone defect in the Z/E@Gel group was predominantly filled with formed bone tissue. This finding

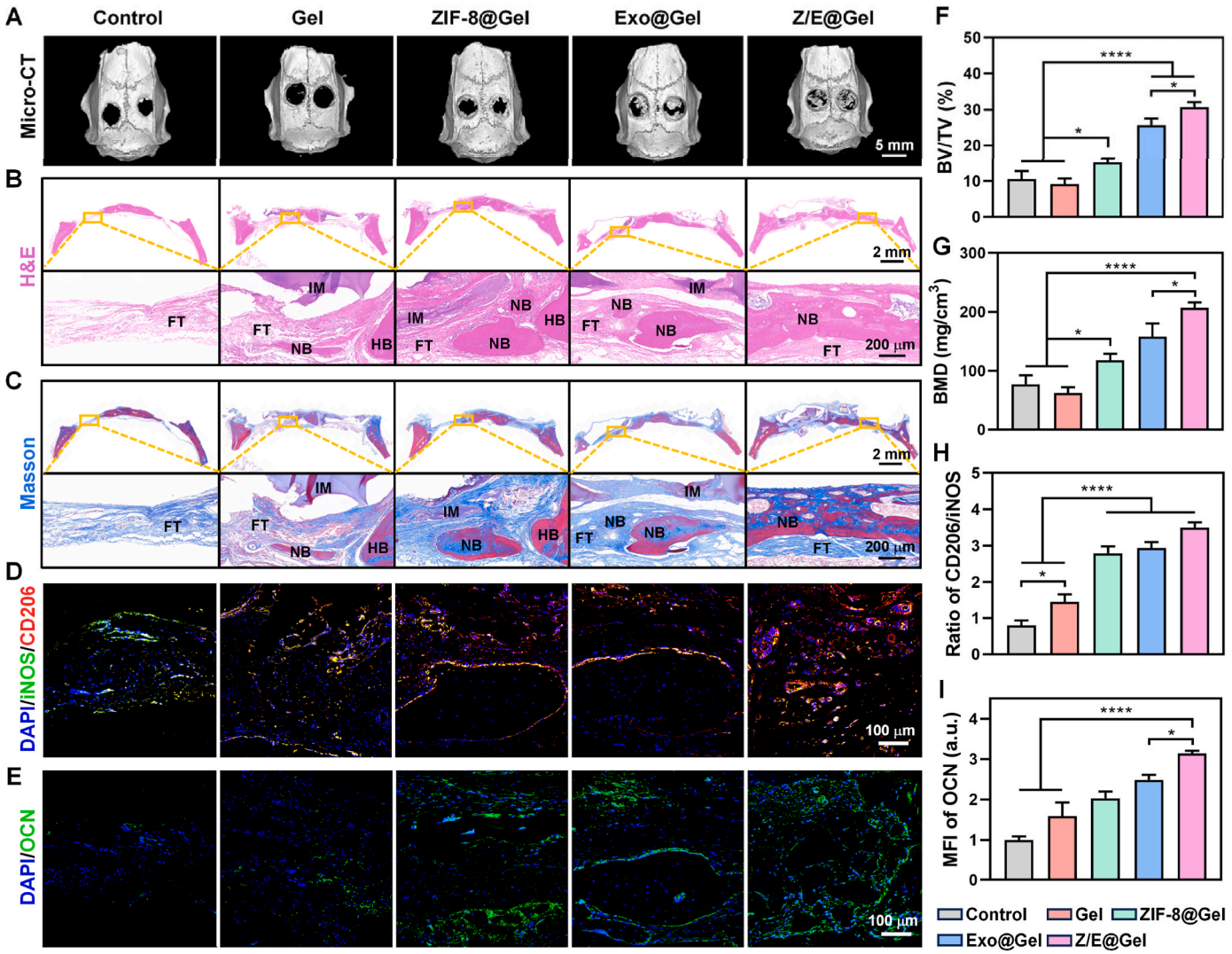

Fig. 9. Evaluation of bone formation *in vivo*. (A) Micro-CT images of bone defects after 8 weeks of implantation. (B) H&E staining of the repaired bone defects (NB: new bone; HB: host bone; IM: implanted material; FT: fibrous tissue). (C) Masson's trichrome staining of the repaired bone defects (NB: new bone; HB: host bone; IM: implanted material; FT: fibrous tissue). (D) Immunofluorescence images of iNOS and CD206 in new bone tissue. (E) Immunofluorescence images of OCN in new bone tissue. (F) Quantitative statistics of BV/TV in the defect area. (G) Quantitative statistics of BMD in the defect area. (H) Quantitative statistics of the ratio of CD206 to iNOS. (I) Quantitative statistics of the expression of OCN in new bone tissue. All data are presented as the mean ± SD (n = 6), *p < 0.05, **p < 0.01, ***p < 0.001, ****p < 0.0001.

indicates that the blank control and pure hydrogel may encounter challenges in repairing critical-sized bone defects, whereas the incorporation of ZIF-8 and MSC-Exos can significantly enhance bone regeneration. Quantitative statistics of bone volume fraction (Fig. 9(F)) and bone mineral density (Fig. 9(G)) demonstrated that ZIF-8@Gel possessed limited osteoinductive capacity, while combining ZIF-8 and MSC-Exos accelerated bone regeneration. The GelMA hydrogel provided optimal spatial support for the adhesion, proliferation, and osteogenic differentiation of BMSCs, while the combined release of zinc ions in ZIF-8 and osteogenic miRNAs in MSC-Exos further promoted the proliferation and mineralization of osteoblasts.

H&E and Masson trichrome staining indicated that the bone defect areas in the ZIF-8@Gel, Exo@Gel, and Z/E@Gel groups were partially filled with new bone tissue, while the center of defect areas in the control group and Gel group were occupied by fibrous tissue (Fig. 9(B, C)). The local magnification images of the defect area indicate the presence of a small amount of undegraded hydrogel in addition to the new bone in the ZIF-8@Gel and Exo@Gel groups. The newly formed bone predominantly exists at the edges of the defect area and gradually extends toward the center to substitute for the hydrogel. Scarcely residual hydrogel could be observed in the Z/E@Gel group, while continuous plate-like bone was formed in the defect area. Immunofluorescence staining for iNOS and CD206 demonstrated that distinct inflammatory markers were present in the fibrous tissue at the defect center of the control group (Fig. 9(D)). Typically, the high expression of iNOS is commonly associated with the infiltration of inflammatory cells and tissue damage [130]. Severe inflammatory responses might result in excessive formation of fibrous tissue, impeding the formation and integration of new bone. It is worth noting that the expression of CD206 was significantly enhanced in the ZIF-8@Gel, Exo@Gel, and Z/E@Gel groups, indicating the excellent anti-inflammatory properties of ZIF-8 and MSC-Exos (Fig. 9(H)).

The *in vivo* experiments indicated that Z/E@Gel has excellent immunomodulatory properties and promotes bone regeneration. Moreover, immunofluorescence staining suggested that the expressions of bone matrix markers OCN, Col I, and Runx2 in the ZIF-8@Gel, Exo@Gel, and Z/E@Gel groups were significantly higher than those in the control group and the Gel group (Fig. 9(E) and Fig. S24A). The Z/E@Gel group demonstrated up-regulated expression levels of osteogenic markers, corresponding to the excellent osteoinductive ability (Fig. 9(I),

Fig. S24B, and Fig. S24C). CD31 is a transmembrane glycoprotein primarily expressed in endothelial cells and significantly influences angiogenesis, cell signaling, and cell migration [131]. As illustrated in Fig. S24(D), the increased expression levels of CD31 in the ZIF-8@Gel, Exo@Gel, and Z/E@Gel groups imply that active angiogenesis is occurring in the nascent tissue to support the growth of the new bone. These results underscore the synergistic capacity of Z/E@Gel to promote osteogenesis, modulate immune responses, and support vascular network development in critical-sized bone defects.

3.10. Comparative analysis with existing work

The regenerative potential of naturally extracted MSC-Exos is influenced by donor cell source, proliferation status, and culture conditions, leading to significant fluctuations in the expression levels of their cargoes, such as miRNAs and growth factors. Since signaling mechanisms within MSCs modulate their exosomal composition, pretreating MSCs to generate engineered exosomes is an effective strategy to enhance the regenerative potential of MSC-Exos. Current pretreatment strategies for MSCs include pharmacological treatment, electrical stimulation, three-dimensional culture, and hypoxia induction. P. Budgude et al. found that pretreatment with a p38 inhibitor restored MSC viability and promoted hematopoietic stem cell expansion via the exosome-mediated Nfya/Cdkn1a axis [132]. M. Lu et al. reported that MSC-Exos induced by quercetin significantly reduced the expression levels of IL-1β-induced proinflammatory markers (MMP9 and COX-2) and restored the expression of cartilage repair genes (SOX9 and type II collagen) in mice with osteoarthritis [133]. J. Chen et al. discovered that MSC-Exos isolated from BMSCs pretreated with electrical stimulation were enriched in proteins involved in "oxidative phosphorylation" regulation, capable of activating bone formation-related PI3K-Akt and MAPK signaling pathways [134]. Compared to the above strategies, the pre-osteogenic differentiation of MSCs employed in this study, which mimics the natural differentiation pathway of bone development *in vitro*, results in exosomes carrying a molecular profile closer to the signaling environment of natural bone tissue repair and reduces interference from non-physiological signals on cells.

Osteogenically induced MSCs can secrete exosomes with enhanced osteogenic effects by altering their miRNA profile, a finding corroborated by numerous previous reports [28,49]. However, previous research has primarily focused on alterations in osteogenic miRNAs within MSC-Exos and their downstream osteogenic differentiation pathways, with less attention paid to the immunomodulatory properties of MSC-Exos. Recently, K. Xiang et al. demonstrated that MSC-Exos derived from three-dimensional culture systems displayed differential expression patterns involving upregulation of 138 miRNAs and downregulation of 347 species, with these transcriptional alterations showing modulatory effects on critical biological pathways including oxidative stress management, angiogenesis regulation, and osteogenic differentiation processes [135]. This work was the first to mention that engineered MSC-Exos could effectively reduce intracellular oxidative stress levels. The study by L. Zhang et al. demonstrated that miR-214–3p carried by bone marrow-derived MSC-Exos could regulate oxidative stress damage and neuronal apoptosis by downregulating CD151 [136]. These findings suggest a potential correlation between exosomal miRNAs and their immunomodulatory properties. Our previous work also found that changes in miR-18a-5p expression in MSC-Exos are key factors influencing their immunomodulatory properties [30]. Indeed, during the differentiation of BMSCs into osteoblasts, the expression of cell surface immunomodulatory molecules and secreted soluble factors is significantly reduced. This occurs because key transcription factors for osteogenic differentiation competitively suppress the promoters of immunomodulatory-related genes; for instance, Runx2 can bind to the IL-10 promoter and inhibit its transcription [137]. Concurrently, the absence of IL-10 can lead to an excessive inflammatory response to environmental challenges and the development of inflammatory diseases [138]. After BMSCs are directionally differentiated into osteoblasts, their metabolic and gene expression networks preferentially serve osteogenic functions, while immunomodulation, as a "non-core function" is actively suppressed. Consequently, in the microenvironment of bone defects with abnormally elevated inflammation levels, MSC-Exos secreted by osteogenically induced BMSCs confront the challenge of deteriorated immunomodulatory properties.

Bone healing is a highly coordinated process involving inflammatory, reparative, and remodeling phases. Excessive or persistent inflammation impedes osteoblast differentiation and new bone formation, while a timely shift towards an anti-inflammatory/reparative microenvironment favors bone regeneration. In recent years, research on MOFs as immunomodulators has garnered increasing attention. C. Zhu et al. reported the application of MOFs as ROS-scavenging nanozymes in the repair of periodontitis [139]. Nanoscale mesoporous UiO-66 type MOF enhanced mitophagy function, promoting the clearance of damaged mitochondria and thereby restoring long-term cellular homeostasis. Y. Xue et al. designed a Zn/Co bimetallic MOF to accelerate diabetic wound healing, utilizing the valence transition of Co^{2+}/Co^{3+} to scavenge ROS and promote the transition of M1 macrophages to the M2 phenotype [140]. G. Li et al. integrated magnesium-gallate (Mg-GA) MOF into a cryogel scaffold for inflammation regulation and bone regeneration promotion [141]. Therein, Mg^{2+} primarily functions in cell recruitment, angiogenesis, and osteogenesis, while GA, as an anti-inflammatory compound, modulates macrophage M1/M2 phenotypes and inhibits osteoclast differentiation. Although existing studies have demonstrated the remarkable immunomodulatory capabilities of MOFs in tissue repair, the underlying molecular mechanisms remain poorly understood. Furthermore, the long-term *in vivo* biocompatibility of MOF materials, their degradation products, and clearance pathways requires in-depth investigation.

In this work, ZIF-8 was introduced as an immunomodulator to enhance the immunomodulatory properties of the composite hydrogel synergistically. The ZIF-8 component within the composite hydrogel exhibited excellent anti-inflammatory properties, effectively reducing ROS expression levels in macrophages under inflammatory conditions and inducing macrophage polarization from the pro-inflammatory M1 phenotype to the anti-inflammatory M2 phenotype. Building on this, we discovered for the first time that ZIF-8 inhibits the activation of the non-canonical NF-κB pathway by suppressing P100 ubiquitination (at K332/K338 sites), proposing a molecular mechanism for MOF-mediated regulation of macrophage polarization. Concurrently, this work compared the immunomodulatory performance differences between ZIF-8 and other MOFs commonly reported in the biomedical field, as shown in Fig. S25. After LPS-induced RAW264.7 cells were incubated with different MOFs, including ZIF-8(Zn), ZIF-67(Co), MOF-74(Mg), MIL-100(Fe), and HKUST-1(Cu), distinct differences in the proportion of M2 polarization were observed (Fig. S26). ZIF-8 and MOF-74 significantly promoted macrophage polarization towards M2, with CD206-positive proportions of 61.56 % and 40.87 %, respectively. In contrast, ZIF-67 and MIL-100 exhibited limited anti-inflammatory properties, with CD206-positive proportions of 28.92 % and 15.50 %, respectively. As a comparison, HKUST-1 scarcely induced M2 polarization.

The immunomodulatory properties of MOFs primarily depend on exposed metal active sites and released metal ions [142]. Zn^{2+} released from ZIF-8 directly affects inflammasome activation by inhibiting Caspase-1 activity, reducing the release of pro-inflammatory factors (e.g., IL-1β, TNF-α), and exerts anti-inflammatory effects by upregulating anti-inflammatory factors like IL-10 [143]. Mg^{2+} suppresses inflammation by blocking the TLR4/NF-κB signaling pathway and enhances mitochondrial oxidative phosphorylation, driving M2 metabolic reprogramming [144]. The dynamic switching of metal ions between +2/+3 valence states in ZIF-67 and MIL-100 exhibits the capacity to initiate Fenton reactions under defined environmental conditions, generating transient ROS elevation that consequently compromises the stability of their immunomodulatory characteristics [145,146]. Due to

the strong cytotoxicity of Cu^{2+}, which can damage mitochondrial function and inhibit cell activity, Cu-based MOFs may exacerbate inflammation-induced oxidative stress, enhance M1 macrophage polarization, and further suppress CD206 expression [147]. Therefore, this paper proposes the use of ZIF-8 as an immunomodulator in bone defect repair, striking a balance between good biocompatibility, immunomodulatory properties, and osteogenic characteristics.

3.11. Innovation and limitations

This work represents the successful co-loading of osteogenically induced MSC-Exos (containing miR-23a-3p) with the immunomodulatory agent ZIF-8 into a GelMA hydrogel. This innovative strategy establishes a zinc ion/exosome sustained-release system capable of simultaneously addressing the critical challenge of "osteo-immunomodulatory imbalance" in bone regeneration. The research elucidates the key regulatory mechanism through which the miR-23a-3p/PTEN/AKT signaling axis governs the osteogenic differentiation of BMSCs, thereby highlighting the targeted therapeutic potential of exosomal miRNAs. Moreover, this work is the first to identify that ZIF-8 inhibits non-classical NF-κB activation by suppressing P100 ubiquitination at K332/K338 sites, proposing a novel molecular mechanism for MOF-mediated regulation of macrophage polarization. Collectively, these findings offer a promising paradigm for designing bone tissue engineering scaffolds that integrate osteoinductive capabilities with immunomodulatory microenvironment remodeling while effectively circumventing the inherent risks associated with stem cell-based therapies.

The current investigation provides robust experimental evidence supporting the synergistic osteogenic and immunomodulatory effects of the MSC-Exos/ZIF-8@GelMA composite hydrogel. Nevertheless, several aspects merit further exploration: Firstly, the UV-crosslinked GelMA hydrogel used in this study is suitable for standard animal experimental models but has operational limitations in the treatment of deep or irregular bone defects. In contrast, injectable composite hydrogel microspheres loaded with exosomes, developed based on microfluidic technology, can be flexibly injected into deep or irregular bone defects [148]. Additionally, alternative strategies such as enzyme-mediated crosslinking, ionic coordination crosslinking, and thermosensitive gel polymers may enhance the clinical applicability of hydrogel scaffolds in complex defects [149,150]. Secondly, this study utilized healthy rat cranial defects as animal models, which cannot reflect common clinical conditions such as osteoporosis, diabetes mellitus, or infectious bone defects. Therefore, systematic evaluation of therapeutic efficacy in these pathological microenvironments is necessary. Furthermore, future *in vivo* studies should assess regenerative capacity under biomechanical loading conditions, as well as large-scale angiogenesis and complex immune responses, using clinically relevant bone defect models in large animals to facilitate the clinical translation of this composite hydrogel platform.

4. Conclusion

In summary, the MSC-Exos and ZIF-8 encapsulated GelMA hydrogel demonstrated favorable biocompatibility *in vitro* and *in vivo* in this study. The composite hydrogel actively induces the polarization of RAW264.7 cells toward the regenerative M2 phenotype, thereby establishing an immune microenvironment conducive to osteogenesis. The sustained release of MSC-Exos and zinc ions within the hydrogel cooperatively facilitates the osteogenic differentiation of BMSCs and the angiogenesis of HUVECs. RNA sequencing and molecular biology experiments demonstrated that ZIF-8 inhibits the activation of non-classical NF-κB signaling pathways in inflammatory settings by decreasing the ubiquitination level of P100 in macrophages, downregulating the expression of inflammatory factors. Meanwhile, the highly expressed miR-23a-3p within MSC-Exos activates the AKT signaling pathway in BMSCs through the targeted silencing of PTEN, thereby facilitating the expression of downstream osteogenesis-related proteins. The critical-sized rat cranial defect model demonstrated that the implanted composite hydrogel effectively reduced inflammation at the defect site and accelerated the formation of new bone tissue and blood vessels. The findings of this study provide valuable guidance for the design of novel regenerative scaffolds for bone tissue engineering.

CRediT authorship contribution statement

Yunhui Si: Writing – original draft, Methodology, Investigation, Formal analysis, Data curation, Conceptualization. **Xiaorong Li:** Writing – original draft, Methodology, Investigation. **Shuao Dong:** Methodology, Formal analysis. **Xueqin Gao:** Methodology. **Yuetong Zhu:** Methodology. **Linzhen Mo:** Methodology. **Zhiwei Wang:** Methodology. **Shuhan Wang:** Writing – review & editing, Supervision. **Chao Zhang:** Writing – review & editing, Supervision, Funding acquisition.

Ethics approval and consent to participate

All animal procedures were approved by the Shenzhen Institute for Drug Control (approval number 20240528). All *in vivo* experiments were conducted in compliance with the Animal Research: Reporting of In Vivo Experiments (ARRIVE) 2.0 guidelines. No human participants were involved in this study.

Declaration of competing interest

The authors declare that they have no known competing financial interests or personal relationships that could have appeared to influence the work reported in this paper.

Acknowledgments

This work was primarily funded by the National Natural Science Foundation of China (grant number: 81971760) and the Guangzhou Key Research and Development Program (grant number: 202206010115).

Appendix A. Supplementary data

Supplementary data to this article can be found online at https://doi.org/10.1016/j.bioactmat.2025.08.026.

References

[1] H. Petite, V. Viateau, W. Bensaid, A. Meunier, C. de Pollak, M. Bourguignon, K. Oudina, L. Sedel, G. Guillemin, Tissue-engineered bone regeneration, Nat. Biotechnol. 18 (9) (2000) 959–963.
[2] J. Wang, Y. Wu, G. Li, F. Zhou, X. Wu, M. Wang, X. Liu, H. Tang, L. Bai, Z. Geng, P. Song, Z. Shi, X. Ren, J. Su, Engineering large-scale self-mineralizing bone organoids with bone matrix-inspired hydroxyapatite hybrid bioinks, Adv. Mater. 36 (30) (2024) e2309875.
[3] C.H. Mac, H.Y. Chan, Y.H. Lin, A.K. Sharma, H.L. Song, Y.S. Chan, K.J. Lin, Y. J. Lin, H.W. Sung, Engineering a biomimetic bone scaffold that can regulate redox homeostasis and promote osteogenesis to repair large bone defects, Biomaterials 286 (2022) 121574.
[4] C. Xie, J. Ye, R. Liang, X. Yao, X. Wu, Y. Koh, W. Wei, X. Zhang, H. Ouyang, Advanced strategies of biomimetic tissue-engineered grafts for bone regeneration, Adv. Healthcare Mater. 10 (14) (2021) e2100408.
[5] L. Lu, X. Liu, Y. Sun, S. Wang, J. Liu, S. Ge, T. Wei, H. Zhang, J. Su, Y. Zhang, W. Fan, Silk-fabric reinforced silk for artificial bones, Adv. Mater. 36 (23) (2024) e2308748.
[6] N. Xue, X. Ding, R. Huang, R. Jiang, H. Huang, X. Pan, W. Min, J. Chen, J. A. Duan, P. Liu, Y. Wang, Bone tissue engineering in the treatment of bone defects, Pharmaceuticals 15 (7) (2022) 879.
[7] X. Yuan, W. Zhu, Z. Yang, N. He, F. Chen, X. Han, K. Zhou, Recent advances in 3D printing of smart scaffolds for bone tissue engineering and regeneration, Adv. Mater. 36 (34) (2024) e2403641.
[8] G.S. Hussey, J.L. Dziki, S.F. Badylak, Extracellular matrix-based materials for regenerative medicine, Nat. Rev. Mater. 3 (7) (2018) 159–173.

[9] Y. Yang, W. Wang, Q. Zeng, N. Wang, W. Li, B. Chen, Q. Guan, C. Li, W. Li, Fabricating oxygen self-supplying 3D printed bioactive hydrogel scaffold for augmented vascularized bone regeneration, Bioact. Mater. 40 (2024) 227–243.
[10] S. Liu, L. Zhang, Z. Li, F. Gao, Q. Zhang, A. Bianco, H. Liu, S. Ge, B. Ma, Materials-mediated in situ physical cues for bone regeneration, Adv. Funct. Mater. 34 (1) (2023).
[11] A. Le Bras, Exosome-based therapy to repair the injured heart, Nat. Rev. Cardiol. 15 (7) (2018) 382.
[12] R. Kalluri, V.S. LeBleu, The biology, function, and biomedical applications of exosomes, Science 367 (6478) (2020) eaau6977.
[13] M.H. Fan, J.K. Pi, C.Y. Zou, Y.L. Jiang, Q.J. Li, X.Z. Zhang, F. Xing, R. Nie, C. Han, H.Q. Xie, Hydrogel-exosome system in tissue engineering: a promising therapeutic strategy, Bioact. Mater. 38 (2024) 1–30.
[14] D. Ha, N. Yang, V. Nadithe, Exosomes as therapeutic drug carriers and delivery vehicles across biological membranes: current perspectives and future challenges, Acta Pharm. Sin. B 6 (4) (2016) 287–296.
[15] K.L. Rock, E. Reits, J. Neefjes, Present yourself! by MHC class I and MHC class II molecules, Trends Immunol. 37 (11) (2016) 724–737.
[16] S.H.S. Tan, J.R.Y. Wong, S.J.Y. Sim, C.K.E. Tjio, K.L. Wong, J.R.J. Chew, J.H. P. Hui, W.S. Toh, Mesenchymal stem cell exosomes in bone regenerative strategies-a systematic review of preclinical studies, Mater. Today Bio 7 (2020) 100067.
[17] J. Huber, M.F. Griffin, M.T. Longaker, N. Quarto, Exosomes: a tool for bone tissue engineering, Tissue Eng., Part B 28 (1) (2022) 101–113.
[18] S.J. Chuah, C.W. Yong, K.Y.W. Teo, J.R.J. Chew, Y.A. Cheow, S. Zhang, R.C. W. Wong, A.A.T. Lim, S.K. Lim, W.S. Toh, Mesenchymal stromal cell-derived small extracellular vesicles modulate macrophage polarization and enhance angio-osteogenesis to promote bone healing, Genes Dis 9 (4) (2022) 841–844.
[19] S. Ren, Y. Lin, W. Liu, L. Yang, M. Zhao, MSC-Exos: important active factor of bone regeneration, Front. Bioeng. Biotechnol. 11 (2023) 1136453.
[20] S. Ma, Y. Zhang, S. Li, A. Li, Y. Li, D. Pei, Engineering exosomes for bone defect repair, Front. Bioeng. Biotechnol. 10 (2022) 1091360.
[21] S. Zhao, G. Xiu, J. Wang, Y. Wen, J. Lu, B. Wu, G. Wang, D. Yang, B. Ling, D. Du, J. Xu, Engineering exosomes derived from subcutaneous fat MSCs specially promote cartilage repair as miR-199a-3p delivery vehicles in osteoarthritis, J. Nanobiotechnol. 21 (1) (2023) 341.
[22] J. Tang, H. Yu, Y. Wang, G. Duan, B. Wang, W. Li, Z. Zhu, miR-27a promotes osteogenic differentiation in glucocorticoid-treated human bone marrow mesenchymal stem cells by targeting PI3K, J. Mol. Histol. 52 (2) (2021) 279–288.
[23] S. Guo, J. Gu, J. Ma, R. Xu, Q. Wu, L. Meng, H. Liu, L. Li, Y. Xu, GATA4-driven miR-206-3p signatures control orofacial bone development by regulating osteogenic and osteoclastic activity, Theranostics 11 (17) (2021) 8379–8395.
[24] G.D. Lu, P. Cheng, T. Liu, Z. Wang, BMSC-Derived exosomal miR-29a promotes angiogenesis and osteogenesis, Front. Cell Dev. Biol. 8 (2020) 608521.
[25] J. Huang, Y. Li, S. Zhu, L. Wang, L. Yang, C. He, MiR-30 family: a novel avenue for treating bone and joint diseases? Int. J. Med. Sci. 20 (4) (2023) 493–504.
[26] L. Yan, D. Li, S. Li, J. Jiao Li, G. Du, H. Liu, J. Zhang, X. Li, Z. Fan, J. Jiu, R. Li, N. Kong, W. Liu, Y. Du, B. Wang, Exosomes derived from 3D-cultured MSCs alleviate knee osteoarthritis by promoting M2 macrophage polarization through miR-365a-5p and inhibiting TLR2/Myd88/NF-κB pathway, Chem. Eng. J. 497 (2024) 154432.
[27] G. Su, X. Lei, Z. Wang, W. Xie, D. Wen, Y. Wu, Mesenchymal stem cell-derived exosomes affect macrophage phenotype: a cell-free strategy for the treatment of skeletal muscle disorders, Curr. Mol. Med. 23 (4) (2023) 350–357.
[28] M. Zhai, Y. Zhu, M. Yang, C. Mao, Human mesenchymal stem cell derived exosomes enhance cell-free bone regeneration by altering their miRNAs profiles, Adv. Sci. 7 (19) (2020) 2001334.
[29] Y. Cui, J. Luan, H. Li, X. Zhou, J. Han, Exosomes derived from mineralizing osteoblasts promote ST2 cell osteogenic differentiation by alteration of microRNA expression, FEBS Lett. 590 (1) (2016) 185–192.
[30] X. Li, Y. Si, J. Liang, M. Li, Z. Wang, Y. Qin, L. Sun, Enhancing bone regeneration and immunomodulation via gelatin methacryloyl hydrogel-encapsulated exosomes from osteogenic pre-differentiated mesenchymal stem cells, J. Colloid Interface Sci. 672 (2024) 179–199.
[31] A. Lotfy, N.M. AboQuella, H. Wang, Mesenchymal stromal/stem cell (MSC)-Derived exosomes in clinical trials, Stem Cell Res. Ther. 14 (1) (2023) 66.
[32] H.N. Kim, A. Jiao, N.S. Hwang, M.S. Kim, D.H. Kang, D.H. Kim, K.Y. Suh, Nanotopography-guided tissue engineering and regenerative medicine, Adv. Drug Deliv. Rev. 65 (4) (2013) 536–558.
[33] K.S. Brammer, C.J. Frandsen, S. Jin, TiO_2 nanotubes for bone regeneration, Trends Biotechnol. 30 (6) (2012) 315–322.
[34] X. Li, X. Shu, Y. Shi, H. Li, X. Pei, MOFs and bone: application of MOFs in bone tissue engineering and bone diseases, Chin. Chem. Lett. 34 (7) (2023) 107986.
[35] B. Tao, W. Zhao, C. Lin, Z. Yuan, Y. He, L. Lu, M. Chen, Y. Ding, Y. Yang, Z. Xia, K. Cai, Surface modification of titanium implants by ZIF-8@Levo/LBL coating for inhibition of bacterial-associated infection and enhancement of in vivo osseointegration, Chem. Eng. J. 390 (2020) 124621.
[36] M. Li, S. Yin, M. Lin, X. Chen, Y. Pan, Y. Peng, J. Sun, A. Kumar, J. Liu, Current status and prospects of metal-organic frameworks for bone therapy and bone repair, J. Mater. Chem. B 10 (27) (2022) 5105–5128.
[37] N. Ren, N. Liang, M. Dong, Z. Feng, L. Meng, C. Sun, A. Wang, X. Yu, W. Wang, J. Xie, C. Liu, H. Liu, Stem cell membrane-encapsulated zeolitic imidazolate framework-8: a targeted nano-platform for osteogenic differentiation, Small 18 (26) (2022) e2202485.
[38] B. Zhang, J. Chen, Z. Zhu, X. Zhang, J. Wang, Advances in immunomodulatory MOFs for biomedical applications, Small 20 (11) (2024) e2307299.
[39] B. Wang, X. Xie, W. Jiang, Y. Zhan, Y. Zhang, Y. Guo, Z. Wang, N. Guo, K. Guo, J. Sun, Osteoinductive micro-nano guided bone regeneration membrane for in situ bone defect repair, Stem Cell Res. Ther. 15 (1) (2024) 135.
[40] Z. Zheng, Y. Chen, B. Guo, Y. Wang, W. Liu, J. Sun, X. Wang, Magnesium-organic framework-based stimuli-responsive systems that optimize the bone microenvironment for enhanced bone regeneration, Chem. Eng. J. 396 (2020) 125241.
[41] Q. Yang, X. Sun, Q. Ding, M. Qi, C. Liu, T. Li, F. Shi, L. Wang, C. Li, J.S. Kim, An ATP-Responsive metal-organic framework against periodontitis via synergistic ion-interference-mediated pyroptosis, Natl. Sci. Rev. 11 (8) (2024) nwae225.
[42] M. Wu, H. Liu, Y. Zhu, P. Wu, Y. Chen, Z. Deng, X. Zhu, L. Cai, Bioinspired soft-hard combined system with mild photothermal therapeutic activity promotes diabetic bone defect healing via synergetic effects of immune activation and angiogenesis, Theranostics 14 (10) (2024) 4014–4057.
[43] Y. Liu, Z. Zhu, X. Pei, X. Zhang, X. Cheng, S. Hu, X. Gao, J. Wang, J. Chen, Q. Wan, ZIF-8-modified multifunctional bone-adhesive hydrogels promoting angiogenesis and osteogenesis for bone regeneration, ACS Appl. Mater. Interfaces 12 (33) (2020) 36978–36995.
[44] H. Zhang, S. Yuan, B. Zheng, P. Wu, X. He, Y. Zhao, Z. Zhong, X. Zhang, J. Guan, H. Wang, L. Yang, X. Zheng, Lubricating and dual-responsive injectable hydrogels formulated from ZIF-8 facilitate osteoarthritis treatment by remodeling the microenvironment, Small 21 (3) (2025) e2407885.
[45] M. Sikora, A. Smieszek, K. Marycz, Bone marrow stromal cells (BMSCs $CD45^-$/$CD44^+$/$CD73^+$/$CD90^+$) isolated from osteoporotic mice SAM/P6 as a novel model for osteoporosis investigation, J. Cell Mol. Med. 25 (14) (2021) 6634–6651.
[46] Y. Si, H. Liu, M. Li, X. Jiang, H. Yu, D. Sun, An efficient metal-organic framework-based drug delivery platform for synergistic antibacterial activity and osteogenesis, J. Colloid Interface Sci. 640 (2023) 521–539.
[47] M. Wang, W. Li, L.S. Mille, T. Ching, Z. Luo, G. Tang, C.E. Garciamendez, A. Lesha, M. Hashimoto, Y.S. Zhang, Digital light processing based bioprinting with composable gradients, Adv. Mater. 34 (1) (2022) e2107038.
[48] Z. Li, H. Dong, S. Yang, X. Wang, Z. Li, An injectable ibuprofen sustained-release composite hydrogel system effectively accelerates diabetic wound healing via anti-inflammatory effects and angiogenesis, Int. J. Nanomed. 20 (2025) 4535–4550.
[49] A. Liu, D. Lin, H. Zhao, L. Chen, B. Cai, K. Lin, S.G. Shen, Optimized BMSC-Derived osteoinductive exosomes immobilized in hierarchical scaffold via lyophilization for bone repair through Bmpr2/Acvr2b competitive receptor-activated smad pathway, Biomaterials 272 (2021) 120718.
[50] J. Chen, X. Zhang, C. Huang, H. Cai, S. Hu, Q. Wan, X. Pei, J. Wang, Osteogenic activity and antibacterial effect of porous titanium modified with metal-organic framework films, J. Biomed. Mater. Res. 105 (3) (2017) 834–846.
[51] X. Gao, Y. Xue, Z. Zhu, J. Chen, Y. Liu, X. Cheng, X. Zhang, J. Wang, X. Pei, Q. Wan, Nanoscale zeolitic imidazolate framework-8 activator of canonical MAPK signaling for bone repair, ACS Appl. Mater. Interfaces 13 (1) (2021) 97–111.
[52] M. Colombo, G. Raposo, C. Théry, Biogenesis, secretion, and intercellular interactions of exosomes and other extracellular vesicles, Annu. Rev. Cell Dev. Biol. 30 (2014) 255–289.
[53] G. van Niel, G. D'Angelo, G. Raposo, Shedding light on the cell biology of extracellular vesicles, Nat. Rev. Mol. Cell Biol. 19 (4) (2018) 213–228.
[54] N. Su, Y. Hao, F. Wang, W. Hou, H. Chen, Y. Luo, Mesenchymal stromal exosome-functionalized scaffolds induce innate and adaptive immunomodulatory responses toward tissue repair, Sci. Adv. 7 (20) (2021) eabf7207.
[55] Y. Cui, B. Lv, Z. Li, C. Ma, Z. Gui, Y. Geng, G. Liu, L. Sang, C. Xu, Q. Min, L. Kong, Z. Zhang, Y. Liu, X. Qi, D. Fu, Bone-targeted biomimetic nanogels Re-establish osteoblast/osteoclast balance to treat postmenopausal osteoporosis, Small 20 (6) (2024) e2303494.
[56] J. He, Y. Sun, Q. Gao, C. He, K. Yao, T. Wang, M. Xie, K. Yu, J. Nie, Y. Chen, Y. He, Gelatin methacryloyl hydrogel, from standardization, performance, to biomedical application, Adv. Healthcare Mater. 12 (23) (2023) e2300395.
[57] L. Deng, Y. Liu, Q. Wu, S. Lai, Q. Yang, Y. Mu, M. Dong, Exosomes to exosome-functionalized scaffolds: a novel approach to stimulate bone regeneration, Stem Cell Res. Ther. 15 (1) (2024) 407.
[58] J.W. Nichol, S.T. Koshy, H. Bae, C.M. Hwang, S. Yamanlar, A. Khademhosseini, Cell-laden microengineered gelatin methacrylate hydrogels, Biomaterials 31 (21) (2010) 5536–5544.
[59] M. Pirmoradian, T. Hooshmand, F. Najafi, M. Haghbin Nazarpak, S. Davaie, Design, synthesis, and characterization of a novel dual cross-linked gelatin-based bioadhesive for hard and soft tissues adhesion capability, Biomed. Mater. 17 (6) (2022) 065010.
[60] S.C. Chao, M.J. Wang, N.S. Pai, S.K. Yen, Preparation and characterization of gelatin-hydroxyapatite composite microspheres for hard tissue repair, Mat. Sci. Eng. C-Mater. 57 (2015) 113–122.
[61] H. Zhang, M. Zhao, Y. Yang, Y.S. Lin, Hydrolysis and condensation of ZIF-8 in water, Microporous Mesoporous Mater. 288 (2019) 109568.
[62] J.H. Yun, H.Y. Lee, S.H. Yeou, J.Y. Jang, C.H. Kim, Y.S. Shin, D.D. D'Lima, Electrostatic attachment of exosome onto a 3D-fabricated calcium silicate/polycaprolactone for enhanced bone regeneration, Mater. Today Bio 29 (2024) 101283.
[63] C. Huang, S. Shi, M. Qin, X. Rong, Z. Ding, X. Fu, W. Zeng, L. Luo, D. Wang, Z. Luo, Y. Li, Z. Zhou, A composite hydrogel functionalized by borosilicate bioactive glasses and VEGF for critical-size bone regeneration, Adv. Sci. 11 (26) (2024) e2400349.
[64] C.R. Kruse, M. Singh, S. Targosinski, I. Sinha, J.A. Sorensen, E. Eriksson, K. Nuutila, The effect of pH on cell viability, cell migration, cell proliferation,

wound closure, and wound reepithelialization: in vitro and in vivo study, Wound Repair Regen. 25 (2) (2017) 260–269.
[65] B.D. Fairbanks, M.P. Schwartz, C.N. Bowman, K.S. Anseth, Photoinitiated polymerization of PEG-Diacrylate with lithium phenyl-2,4,6-trimethylbenzoylphosphinate: polymerization rate and cytocompatibility, Biomaterials 30 (35) (2009) 6702–6707.
[66] N.M. Astakhova, A.V. Korel, E.I. Shchelkunova, K.E. Orishchenko, S.V. Nikolaev, U.S. Zubairova, I.A. Kirilova, Analysis of the basic characteristics of osteogenic and chondrogenic cell lines important for tissue engineering implants, Bull. Exp. Biol. Med. 164 (4) (2018) 561–568.
[67] Z. Guo, C. Yang, Z. Zhou, S. Chen, F. Li, Characterization of biodegradable poly (lactic acid) porous scaffolds prepared using selective enzymatic degradation for tissue engineering, RSC Adv. 7 (54) (2017) 34063–34070.
[68] Y. Ai, C. Guo, M. Garcia-Contreras, B.L. Sanchez, A. Saftics, O. Shodubi, S. Raghunandan, J. Xu, S.J. Tsai, Y. Dong, R. Li, T. Jovanovic-Talisman, S. J. Gould, Endocytosis blocks the vesicular secretion of exosome marker proteins, Sci. Adv. 10 (19) (2024) eadi9156.
[69] S. Pfeiler, M. Thakur, P. Grunauer, R.T.A. Megens, U. Joshi, R. Coletti, V. Samara, G. Müller-Stoy, H. Ishikawa-Ankerhold, K. Stark, A. Klingl, T. Fröhlich, G. J. Arnold, S. Wördemann, C.J. Bruns, H. Algül, C. Weber, S. Massberg, B. Engelmann, CD36-triggered cell invasion and persistent tissue colonization by tumor microvesicles during metastasis, FASEB J. 33 (2) (2019) 1860–1872.
[70] Q. Chen, Y. Li, W. Gao, L. Chen, W. Xu, X. Zhu, Exosome-mediated crosstalk between tumor and tumor-associated macrophages, Front. Mol. Biosci. 8 (2021) 764222.
[71] W. Liu, L. Li, Y. Rong, D. Qian, J. Chen, Z. Zhou, Y. Luo, D. Jiang, L. Cheng, S. Zhao, F. Kong, J. Wang, Z. Zhou, T. Xu, F. Gong, Y. Huang, C. Gu, X. Zhao, J. Bai, F. Wang, W. Zhao, L. Zhang, X. Li, G. Yin, J. Fan, W. Cai, Hypoxic mesenchymal stem cell-derived exosomes promote bone fracture healing by the transfer of miR-126, Acta Biomater. 103 (2020) 196–212.
[72] Y. Ge, J. Wu, L. Zhang, N. Huang, Y. Luo, A new strategy for the regulation of neuroinflammation: exosomes derived from mesenchymal stem cells, cell, Mol. Neurobiol. 44 (1) (2024) 24.
[73] Z. Jiang, Y. Zhang, Y. Zhang, Z. Jia, Z. Zhang, J. Yang, Cancer derived exosomes induce macrophages immunosuppressive polarization to promote bladder cancer progression, Cell Commun. Signal. 19 (1) (2021) 93.
[74] D. Feng, W.L. Zhao, Y.Y. Ye, X.C. Bai, R.Q. Liu, L.F. Chang, Q. Zhou, S.F. Sui, Cellular internalization of exosomes occurs through phagocytosis, Traffic 11 (5) (2010) 675–687.
[75] T. Tian, Y.L. Zhu, F.H. Hu, Y.Y. Wang, N.P. Huang, Z.D. Xiao, Dynamics of exosome internalization and trafficking, J. Cell. Physiol. 228 (7) (2013) 1487–1495.
[76] J. Zhang, W. Zhang, J. Dai, X. Wang, S.G. Shen, Overexpression of Dlx2 enhances osteogenic differentiation of BMSCs and MC3T3-E1 cells via direct upregulation of osteocalcin and alp, Int. J. Oral Sci. 11 (2) (2019) 12.
[77] J. Na, Z. Yang, Q. Shi, C. Li, Y. Liu, Y. Song, X. Li, L. Zheng, Y. Fan, Extracellular matrix stiffness as an energy metabolism regulator drives osteogenic differentiation in mesenchymal stem cells, bioact, Mater 35 (2024) 549–563.
[78] T. Komori, Functions of osteocalcin in bone, pancreas, testis, and muscle, Int. J. Mol. Sci. 21 (20) (2020) 7513.
[79] R. Naomi, P.M. Ridzuan, H. Bahari, Current insights into collagen type I, Polymers 13 (16) (2021) 2642.
[80] Z. Liu, H. Liu, S. Liu, B. Li, Y. Liu, E. Luo, SIRT1 activation promotes bone repair by enhancing the coupling of type H vessel formation and osteogenesis, Cell Prolif. 57 (6) (2024) e13596.
[81] J. Li, J. Ma, Q. Feng, E. Xie, Q. Meng, W. Shu, J. Wu, L. Bian, F. Han, B. Li, Building osteogenic microenvironments with a double-network composite hydrogel for bone repair, Research 6 (2023) 21.
[82] K. Zha, W. Hu, Y. Xiong, S. Zhang, M. Tan, P. Bu, Y. Zhao, W. Zhang, Z. Lin, Y. Hu, M.A. Shahbazi, Q. Feng, G. Liu, B. Mi, Nanoarchitecture-integrated hydrogel boosts angiogenesis-osteogenesis-neurogenesis tripling for infected bone fracture healing, Adv. Sci. 11 (43) (2024) e2406439.
[83] L. Chen, C. Yu, Y. Xiong, K. Chen, P. Liu, A.C. Panayi, X. Xiao, Q. Feng, B. Mi, G. Liu, Multifunctional hydrogel enhances bone regeneration through sustained release of stromal cell-derived Factor-1α and exosomes, Bioact. Mater. 25 (2023) 460–471.
[84] J. Tan, S. Li, C. Sun, G. Bao, M. Liu, Z. Jing, H. Fu, Y. Sun, Q. Yang, Y. Zheng, X. Wang, H. Yang, A dose-dependent spatiotemporal response of angiogenesis elicited by Zn biodegradation during the initial stage of bone regeneration, Adv. Healthcare Mater. 13 (4) (2024) e2302305.
[85] B. Yue, H. Yang, J. Wang, W. Ru, J. Wu, Y. Huang, X. Lan, C. Lei, H. Chen, Exosome biogenesis, secretion and function of exosomal miRNAs in skeletal muscle myogenesis, Cell Prolif. 53 (7) (2020) e12857.
[86] R. Garcia-Martin, G. Wang, B.B. Brandao, T.M. Zanotto, S. Shah, S. Kumar Patel, B. Schilling, C.R. Kahn, MicroRNA sequence codes for small extracellular vesicle release and cellular retention, Nature 601 (7893) (2022) 446–451.
[87] J.F. Xu, G.H. Yang, X.H. Pan, S.J. Zhang, C. Zhao, B.S. Qiu, H.F. Gu, J.F. Hong, L. Cao, Y. Chen, B. Xia, Q. Bi, Y.P. Wang, Altered microRNA expression profile in exosomes during osteogenic differentiation of human bone marrow-derived mesenchymal stem cells, PLoS One 9 (12) (2014) e114627.
[88] C. Jin, L. Jia, Z. Tang, Y. Zheng, Long non-coding RNA MIR22HG promotes osteogenic differentiation of bone marrow mesenchymal stem cells via PTEN/AKT pathway, cell death, Dis 11 (7) (2020) 601.
[89] H. Zhang, Z. Wang, Q. Li, C. Cao, Y. Guo, Y. Chen, IRTKS promotes osteogenic differentiation by inhibiting PTEN phosphorylation, Biomed. Pharmacother. 177 (2024) 116872.
[90] H. Zheng, J. Liu, E. Tycksen, R. Nunley, A. McAlinden, MicroRNA-181a/b-1 over-expression enhances osteogenesis by modulating PTEN/PI3K/AKT signaling and mitochondrial metabolism, Bone 123 (2019) 92–102.
[91] L. Qi, S. Hong, T. Zhao, J. Yan, W. Ge, J. Wang, X. Fang, W. Jiang, S.G. Shen, L. Zhang, DNA tetrahedron delivering miR-21-5p promotes senescent bone defects repair through synergistic regulation of osteogenesis and angiogenesis, Adv. Healthcare Mater. 13 (30) (2024) e2401275.
[92] Z. Zhang, Y. Guo, X. Gao, X. Wang, C. Jin, Role of histone methyltransferase KMT2D in BMSC osteogenesis via AKT signaling, Regen. Ther. 26 (2024) 775–782.
[93] D. Jiao, A. Zheng, Y. Liu, X. Zhang, X. Wang, J. Wu, W. She, K. Lv, L. Cao, X. Jiang, Bidirectional differentiation of BMSCs induced by a biomimetic procallus based on a gelatin-reduced graphene oxide reinforced hydrogel for rapid bone regeneration, Bioact. Mater. 6 (7) (2021) 2011–2028.
[94] S. Rokutanda, T. Fujita, N. Kanatani, C.A. Yoshida, H. Komori, W. Liu, A. Mizuno, T. Komori, Akt regulates skeletal development through GSK3, mTOR, and FoxOs, Dev. Biol. 328 (1) (2009) 78–93.
[95] L. Wan, Y. Wang, J. Li, Y. Wang, H. Zhang, Inhibition of the AKT/mTOR pathway negatively regulates PTEN expression via miRNAs, acta bioch, Bioph. Sin. 54 (11) (2022) 1637–1647.
[96] Y.R. Lee, M. Chen, P.P. Pandolfi, The functions and regulation of the PTEN tumour suppressor: new modes and prospects, Nat. Rev. Mol. Cell Biol. 19 (9) (2018) 547–562.
[97] X. Ge, M. Li, J. Yin, Z. Shi, Y. Fu, N. Zhao, H. Chen, L. Meng, X. Li, Z. Hu, X. Zhao, H. Guo, X. Qian, Fumarate inhibits PTEN to promote tumorigenesis and therapeutic resistance of type2 papillary renal cell carcinoma, Mol. Cell 82 (7) (2022) 1249–1260.
[98] T. Chen, S. Xie, J. Cheng, Q. Zhao, H. Wu, P. Jiang, W. Du, AKT1 phosphorylation of cytoplasmic ME2 induces a metabolic switch to glycolysis for tumorigenesis, Nat. Commun. 15 (1) (2024) 686.
[99] J. Lorenz, S. Richter, A.S. Kirstein, F. Kolbig, M. Nebe, M. Schulze, W. Kiess, I. Spitzbarth, N. Kloting, D. Le Duc, U. Baschant, A. Garten, Pten knockout in mouse preosteoblasts leads to changes in bone turnover and strength, JBMR Plus 8 (3) (2024) ziad016.
[100] T.A. Einhorn, L.C. Gerstenfeld, Fracture healing: mechanisms and interventions, Nat. Rev. Rheumatol. 11 (1) (2015) 45–54.
[101] C. Zhao, Z. Yang, Y. Li, Z. Wen, Macrophages in tissue repair and regeneration: insights from zebrafish, Cell Regen. 13 (1) (2024) 12.
[102] Z. Chi, S. Chen, D. Yang, W. Cui, Y. Lu, Z. Wang, M. Li, W. Yu, J. Zhang, Y. Jiang, R. Sun, Q. Yu, T. Hu, X. Lu, Q. Deng, Y. Yang, T. Zhao, M. Chang, Y. Li, X. Zhang, M. Shang, Q. Xiao, K. Ding, D. Wang, Gasdermin D-mediated metabolic crosstalk promotes tissue repair, Nature 634 (8036) (2024) 1168–1177.
[103] J. Zhang, K. Akiyama, A.Y. Mun, R. Tagashira, T. Zou, N. Matsunaga, T. Kohno, T. Kuboki, Age-related effects on MSC immunomodulation, macrophage polarization, apoptosis, and bone regeneration correlate with IL-38 expression, Int. J. Mol. Sci. 25 (6) (2024) 3252.
[104] E. Olmsted-Davis, J. Mejia, E. Salisbury, Z. Gugala, A.R. Davis, A population of M2 macrophages associated with bone formation, Front. Immunol. 12 (2021) 686769.
[105] M. Locati, G. Curtale, A. Mantovani, Diversity, mechanisms, and significance of macrophage plasticity, Annu. Rev. Pathol. 15 (2020) 123–147.
[106] M.C. Bosco, Macrophage polarization: reaching across the aisle? J. Allergy Clin. Immunol. 143 (4) (2019) 1348–1350.
[107] H. Sun, J. Xu, Y. Wang, S. Shen, X. Xu, L. Zhang, Q. Jiang, Bone microenvironment regulative hydrogels with ROS scavenging and prolonged oxygen-generating for enhancing bone repair, Bioact. Mater. 24 (2023) 477–496.
[108] A. Cammarata-Mouchtouris, A. Acker, A. Goto, D. Chen, N. Matt, V. Leclerc, Dynamic regulation of NF-κB response in innate immunity: the case of the IMD pathway in drosophila, Biomedicines 10 (9) (2022) 2304.
[109] S. Lv, J. Li, X. Qiu, W. Li, C. Zhang, Z.N. Zhang, B. Luan, A negative feedback loop of ICER and NF-κB regulates TLR signaling in innate immune responses, Cell Death Differ. 24 (3) (2017) 492–499.
[110] B.L. Lampson, A.S. Ramiotarez, M. Baro, L. He, M. Hegde, V. Koduri, J.L. Pfaff, R. E. Hanna, J. Kowal, N.H. Shirole, Y. He, J.G. Doench, J.N. Contessa, K.P. Locher, W.G. Kaelin Jr., Positive selection CRISPR screens reveal a druggable pocket in an oligosaccharyltransferase required for inflammatory signaling to NF-κB, Cell 187 (9) (2024) 2209–2223.
[111] M. Son, T. Frank, T. Holst-Hansen, A.G. Wang, M. Junkin, S.S. Kashaf, A. Trusina, S. Tay, Spatiotemporal NF-κB dynamics encodes the position, amplitude, and duration of local immune inputs, Sci. Adv. 8 (35) (2022) eabn6240.
[112] M.G. Dorrington, I.D.C. Fraser, NF-κB signaling in macrophages: dynamics, crosstalk, and signal integration, Front. Immunol. 10 (2019) 705.
[113] A.J. Fusco, A. Mazumder, V.Y. Wang, Z. Tao, C. Ware, G. Ghosh, The NF-κB subunit RelB controls p100 processing by competing with the kinases NIK and IKK1 for binding to p100, Sci. Signal. 9 (447) (2016) ra96.
[114] Y. Li, J.Y. Yang, X. Xie, Z. Jie, L. Zhang, J. Shi, D. Lin, M. Gu, X. Zhou, H.S. Li, S. S. Watowich, A. Jain, S. Yun Jung, J. Qin, X. Cheng, S.C. Sun, Preventing abnormal NF-κB activation and autoimmunity by Otub1-mediated p100 stabilization, Cell Res. 29 (6) (2019) 474–485.
[115] B. Chatterjee, P. Roy, U.A. Sarkar, M. Zhao, Y. Ratra, A. Singh, M. Chawla, S. De, J. Gomes, R. Sen, S. Basak, Immune differentiation regulator p100 tunes NF-κB responses to TNF, Front. Immunol. 10 (2019) 997.
[116] B. Chen, C. Li, J. Yao, L. Shi, W. Liu, F. Wang, S. Huo, Y. Zhang, Y. Lu, U. Ashraf, J. Ye, X. Liu, Zebrafish NIK mediates IFN induction by regulating activation of IRF3 and NF-κB, J. Immunol. 204 (7) (2020) 1881–1891.

[117] S.C. Sun, The noncanonical NF-κB pathway, Immunol. Rev. 246 (1) (2012) 125–140.
[118] M. Chen, Z. Zhao, Q. Meng, P. Liang, Z. Su, Y. Wu, J. Huang, J. Cui, TRIM14 promotes noncanonical NF-κB activation by modulating p100/p52 stability via selective autophagy, Adv. Sci. 7 (1) (2020) 1901261.
[119] T. Huang, G. Yan, M. Guan, Zinc homeostasis in bone: zinc transporters and bone diseases, Int. J. Mol. Sci. 21 (4) (2020) 1236.
[120] Z.S. Zang, Y.M. Xu, A.T.Y. Lau, Molecular and pathophysiological aspects of metal ion uptake by the zinc transporter ZIP8 (SLC39A8), Toxicol. Res. 5 (4) (2016) 987–1002.
[121] H. Gao, W. Dai, L. Zhao, J. Min, F. Wang, The role of zinc and zinc homeostasis in macrophage function, J. Immunol. Res. 2018 (2018) 6872621.
[122] W. Bal, M. Sokolowska, E. Kurowska, P. Faller, Binding of transition metal ions to albumin: sites, affinities and rates, Biochim. Biophys. Acta 1830 (12) (2013) 5444–5455.
[123] D. Zhang, Y. Dang, R. Deng, Y. Ma, J. Wang, J. Ao, X. Wang, Research progress of macrophages in bone regeneration, J. Tissue Eng. Regen. Med. 2023 (2023) 1512966.
[124] M. Gou, H. Wang, H. Xie, H. Song, Macrophages in guided bone regeneration: potential roles and future directions, Front. Immunol. 15 (2024) 1396759.
[125] P.V. Giannoudis, D. Hak, D. Sanders, E. Donohoe, T. Tosounidis, C. Bahney, Inflammation, bone healing, and anti-inflammatory drugs: an update, J. Orthop. Trauma 29 (Suppl 12) (2015) S6–S9.
[126] K.P. Sundararaj, D.J. Samuvel, Y. Li, J.J. Sanders, M.F. Lopes-Virella, Y. Huang, Interleukin-6 released from fibroblasts is essential for up-regulation of matrix metalloproteinase-1 expression by U937 macrophages in coculture: cross-talking between fibroblasts and U937 macrophages exposed to high glucose, J. Biol. Chem. 284 (20) (2009) 13714–13724.
[127] T. Ishijima, K. Nakajima, Inflammatory cytokines TNFα, IL-1β, and IL-6 are induced in endotoxin-stimulated microglia through different signaling cascades, Sci. Prog. 104 (4) (2021) 368504211054985.
[128] P. Behrendt, A. Preusse-Prange, T. Klüter, M. Haake, B. Rolauffs, A.J. Grodzinsky, S. Lippross, B. Kurz, IL-10 reduces apoptosis and extracellular matrix degradation after injurious compression of mature articular cartilage, Osteoarthr. Cartil. 24 (11) (2016) 1981–1988.
[129] Y. Xiong, C. Yan, L. Chen, Y. Endo, Y. Sun, W. Zhou, Y. Hu, L. Hu, D. Chen, H. Xue, B. Mi, G. Liu, IL-10 induces MC3T3-E1 cells differentiation towards osteoblastic fate in murine model, J. Cell Mol. Med. 24 (1) (2020) 1076–1086.
[130] K.K. Wu, X. Xu, M. Wu, X. Li, M. Hoque, G.H.Y. Li, Q. Lian, K. Long, T. Zhou, H. Piao, A. Xu, H.X. Hui, K.K. Cheng, MDM2 induces pro-inflammatory and glycolytic responses in M1 macrophages by integrating iNOS-nitric oxide and HIF-1α pathways in mice, Nat. Commun. 15 (1) (2024) 8624.
[131] S.L. Natividad-Diaz, S. Browne, A.K. Jha, Z. Ma, S. Hossainy, Y.K. Kurokawa, S. C. George, K.E. Healy, A combined hiPSC-derived endothelial cell and in vitro microfluidic platform for assessing biomaterial-based angiogenesis, Biomaterials 194 (2019) 73–83.
[132] P. Budgude, V. Kale, A. Vaidya, Microvesicles and exosomes isolated from murine bone marrow-derived mesenchymal stromal cells primed with p38MAPK inhibitor differentially regulate hematopoietic stem cell function, Artif. Cells, Nanomed. Biotechnol. 53 (1) (2025) 122–137.
[133] M. Lu, A. Lou, J. Gao, S. Li, L. He, W. Fan, L. Zhao, Quercetin-primed MSC exosomes synergistically attenuate osteoarthritis progression, J. Orthop. Surg. Res. 20 (1) (2025) 373.
[134] J. Chen, J. Chen, J. Chen, R. Lu, Z. Liu, Y. Zhang, C. Zhang, Pretreated exosomes by electrical stimulation accelerate bone regeneration, Bioact. Mater. 51 (2025) 383–398.
[135] K. Xiang, M. Hao, Z. Zhang, K. Zhang, H. Sun, L. Zhang, Engineering 3D-BMSC exosome-based hydrogels that collaboratively regulate bone microenvironment and promote osteogenesis for enhanced cell-free bone regeneration, Mater. Today Bio 32 (2025) 101881.
[136] L. Zhang, MicroRNA-214-3p delivered by bone marrow mesenchymal stem cells-secreted exosomes affects oxidative stress in alzheimer's disease rats by targeting CD151, Organogenesis 21 (1) (2025) 2489673.
[137] G. Holdsworth, J.R. Staley, P. Hall, I. van Koeverden, C. Vangjeli, R. Okoye, R. W. Boyce, J.R. Turk, M. Armstrong, A. Wolfreys, G. Pasterkamp, Sclerostin downregulation globally by naturally occurring genetic variants, or locally in atherosclerotic plaques, does not associate with cardiovascular events in humans, J. Bone Miner. Res. 36 (7) (2021) 1326–1339.
[138] B. Mishra, M. Bachu, R. Yuan, C. Wingert, V. Chaudhary, C. Brauner, R. Bell, L. B. Ivashkiv, IL-10 targets IRF transcription factors to suppress IFN and inflammatory response genes by epigenetic mechanisms, Nat. Immunol. 26 (5) (2025) 748–759.
[139] C. Zhu, K. Huang, T. Li, Y. Li, Y. Jin, R. Li, Z. Zhu, S. Yang, L. Xia, B. Fang, Manganese dioxide coupled metal-organic framework as mitophagy regulator alleviates periodontitis through SIRT1-FOXO3-BNIP3 signaling axis, Biomaterials 319 (2025) 123179.
[140] Y. Xue, L. Zhang, J. Chen, D. Ma, Y. Zhang, Y. Han, An "all-in-one" therapeutic platform for programmed antibiosis, immunoregulation and neuroangiogenesis to accelerate diabetic wound healing, Biomaterials 321 (2025) 123293.
[141] G. Li, Y. Wang, Y. Pang, X. Wang, X. Li, H. Leng, Y. Yu, X. Yang, Q. Cai, Magnesium-gallate MOF integrated conductive cryogel for inflammation regulation and boosting bone regeneration, Int. J. Biol. Macromol. 306 (2025) 141672.
[142] F. Wang, H. Yao, X. Wu, Y. Tang, Y. Bai, H. Chong, H. Pang, Metal-organic framework and its composites modulate macrophage polarization in the treatment of inflammatory diseases, Chin. Chem. Lett. 35 (5) (2024) 108821.
[143] X. Gong, W. Gu, S. Fu, G. Zou, Z. Jiang, Zinc homeostasis regulates caspase activity and inflammasome activation, PLoS Pathog. 20 (12) (2024) e1012805.
[144] L. Liang, D. Song, K. Wu, Z. Ouyang, Q. Huang, G. Lei, K. Zhou, J. Xiao, H. Wu, Sequential activation of M1 and M2 phenotypes in macrophages by Mg degradation from Ti-Mg alloy for enhanced osteogenesis, Biomater. Res. 26 (1) (2022) 17.
[145] Z. Salloum, E.A. Lehoux, M.E. Harper, I. Catelas, Effects of cobalt and chromium ions on oxidative stress and energy metabolism in macrophages in vitro, J. Orthop. Res. 36 (12) (2018) 3178–3187.
[146] J. Tang, J. Wang, Fenton-like degradation of sulfamethoxazole using Fe-based magnetic nanoparticles embedded into mesoporous carbon hybrid as an efficient catalyst, Chem. Eng. J. 351 (2018) 1085–1094.
[147] S. Zangiabadi, K.P. Chamoun, K. Nguyen, Y. Tang, G. Sweeney, A.A. Abdul-Sater, Copper infused fabric attenuates inflammation in macrophages, PLoS One 18 (9) (2023) e0287741.
[148] Y. Si, S. Dong, M. Li, J. Gu, M. Luo, X. Wang, Z. Wang, X. Li, C. Zhang, Curcumin-encapsulated exosomes in bisphosphonate-modified hydrogel microspheres promote bone repair through macrophage polarization and DNA damage mitigation, Mater. Today Bio 32 (2025) 101874.
[149] F. Miao, T. Liu, X. Zhang, X. Wang, Y. Wei, Y. Hu, X. Lian, L. Zhao, W. Chen, D. Huang, Engineered bone tissues using biomineralized gelatin methacryloyl/sodium alginate hydrogels, J. Biomater. Sci. Polym. Ed. 33 (2) (2022) 137–154.
[150] S. Saravanan, S. Vimalraj, P. Thanikaivelan, S. Banudevi, G. Manivasagam, A review on injectable chitosan/beta glycerophosphate hydrogels for bone tissue regeneration, Int. J. Biol. Macromol. 121 (2019) 38–54.